Fracture properties of austenitic stainless steel grain boundaries oxidized in PWR environment

Rachma Azihari, Marc Legros, Jeremy Hure, Benoît Tanguy

To cite this version:

Rachma Azihari, Marc Legros, Jeremy Hure, Benoît Tanguy. Fracture properties of austenitic stainless steel grain boundaries oxidized in PWR environment. Acta Materialia, 2024, 278, pp.120175. ⟨10.1016/j.actamat.2024.120175⟩. ⟨cea-05442696⟩

HAL Id: cea-05442696
https://cea.hal.science/cea-05442696v1

Submitted on 15 Jan 2026

Fracture properties of austenitic stainless steel grain boundaries oxidized in PWR environment

R. Azihari[a,b], M. Legros[b], J. Hure[a], B. Tanguy[a]

[a] *Université Paris-Saclay, CEA, Service d'Étude des Matériaux Irradiés, 91191, Gif-sur-Yvette, France*
[b] *CEMES-CNRS and Université de Toulouse, 29 rue Jeanne Marvig, 31055, Toulouse, France*

Abstract

In this study, the fracture properties of a $FeCr_{12}Ni_{26}Si_3$ (wt %) austenitic stainless steel grain boundaries (GB) oxidized in Pressurized Water Reactor (PWR) environment are assessed. The alloy chemical composition mimics the composition of 304 / 316 stainless steels GBs after irradiation, making the results obtained relevant for Irradiation-Assisted Stress Corrosion Cracking (IASCC). Oxidation tests have been performed in nominal PWR environment for 3680h and 7470h. The oxidized samples have been characterized through Scanning Electron Microscope (SEM) and Transmission Electron Microscope (TEM) to quantify the chemical compositions and thicknesses of bulk and intergranular oxides. Micro-cantilevers beams containing a single grain boundary have been milled on oxidized samples using Focused Ion Beam (FIB) and tested in-situ SEM at room temperature. Intergranular cracking has been observed in 12 micro-beams, either within the GB oxide or at the oxide / metal interface. The Coupled Criterion (CC) theoretical framework for crack nucleation has first been used to obtain estimates of the fracture properties. These estimates have then been refined by comparing the experimental results to Finite Element (FE) simulations using Cohesive Zone Model (CZM). A good agreement for the macroscopic fracture load is obtained with a fracture energy $\gamma_c \approx 11 \pm 3\text{J.m}^{-2}$ and a strength $\sigma_c \approx 1000 \pm 250\text{MPa}$ of the oxide. These values are finally compared to the results available in the literature, as well as critically assessed with respect to their dependence to the experimental and numerical parameters.

Keywords: Austenitic stainless steel, Oxidation, PWR environment, Intergranular cracking, Grain boundary fracture properties

---

1. Introduction

InterGranular Stress Corrosion Cracking (IGSCC) is a degradation phenomenon observed for a wide range of materials and applications [1, 2]. After an incubation phase, cracks initiate and propagate along grain boundaries (GB) [3, 4] as a result of the interaction between the material corrosion susceptibility, the corrosive environment and the mechanical loading. IGSCC occurrences are observed in materials used in nuclear power plants [5, 6] such as Ni-based alloys used in steam generators [7, 8] and austenitic steels used for structural applications [9, 10]. Focusing on austenitic stainless steels used in Pressurized Water Reactors (PWR), IGSCC has been reported numerous times in primary and secondary circuits, for example in cold worked materials [11] or in situations involving a pollution of the environment and / or occluded conditions [12]. Recent occurrences include safety injection system piping [13] and baffle-former bolts of the reactor core internal structures [14]. The latter case is specifically referred to as Irradiation-Assisted Stress Corrosion Cracking (IASCC) [15, 16]. Irradiation creates changes in the microstructure such as Frank dislocation loops, black dots, precipitates [17] as well as changes of chemical composition at GBs called Radiation Induced Segregation (RIS) [18]. These changes affect both the mechanical behavior - through irradiation-induced hardening [19] and changes in deformation mechanisms [20] - and the oxidation behavior [21, 22], leading to an increase in the susceptibility of austenitic stainless steels to IGSCC.

---

[*] Corresponding authors: rachma.azihari@outlook.com, marc.legros@cemes.fr, jeremy.hure@cea.fr, benoit.tanguy@cea.fr

A key milestone towards the modeling of IGSCC / IASCC for austenitic stainless steels is the quantitative prediction of crack initiation. Several modeling strategies have been proposed in the literature. Some of these models aim at predicting fracture initiation at the component scale, *i.e.*, providing macroscopic load and time to failure. Dose-dependent stress thresholds under which IGSCC is unlikely were also elaborated for irradiated austenitic stainless steels [23, 24]. Similarly, probabilistic models to estimate the time of IGSCC initiation were recently proposed for such irradiated austenitic stainless steels [25, 26]. However, these models heavily rely on experimental data obtained on neutron irradiated materials tested in shielded autoclaves for calibration. Physically-based models have been proposed to overcome this issue and to predict cracking initiation at the microstructure scale. Basically, these models combine local stress / strain fields at the grain boundaries and a local fracture criterion to predict IG crack initiation. Prediction of intergranular stresses can be either analytical or numerical. In the latter case, polycrystalline aggregates simulations have been refined over the years [27, 28] benefiting from advances on crystal plasticity constitutive equations [29]. This approach has been used to assess local stress criteria for crack nucleation for unirradiated and irradiated austenitic stainless steels, using analytical [30, 31] or numerical [32, 33, 34, 35] predictions of local stress fields. For highly irradiated materials where the dislocation channelling deformation mechanism is dominant, a similar approach has been proposed which considers stresses at the interface between dislocation channels and grain boundaries [36, 37]. An intermediate modeling approach between phenomenological component scale models and physically-based microstructure scale models has also been proposed [38, 39] where component scale simulations results are used as inputs of microstructure scale estimations of local strain / stress fields.

All studies reported hereabove at the microstructure scale require a GB cracking criterion. Some of them use a critical stress criterion [35] while others use a coupled criterion based on both fracture energy and fracture strength [37]. Only a few works have been devoted to the determination of the fracture properties of austenitic stainless steel grain boundaries oxidized in PWR environment. A duplex oxide layer is typically formed with a Fe-rich discontinuous outer layer and Cr-rich continuous inner layer [22]. The inner layer, that extends deeper at grain boundaries [40, 41], has a spinel structure of composition $(\mathrm{Ni_x}, \mathrm{Fe_{1-x}})\mathrm{Cr_2O_4}$. The room temperature fracture properties of this type of oxyde have been predicted theoretically [42], leading to a fracture energy of about $11\mathrm{J.m^{-2}}$ for $\mathrm{FeCr_2O_4}$ and $3\mathrm{J.m^{-2}}$ for $\mathrm{NiCr_2O_4}$, and a strength of about 27GPa for $\mathrm{FeCr_2O_4}$ and 10GPa for $\mathrm{NiCr_2O_4}$. These values are in qualitative agreement with results obtained using Molecular Dynamics (MD) simulations [43] that lead to a fracture energy $\gamma_c \in [2-6]\mathrm{J.m^{-2}}$ and a strength $\sigma_c \in [9-14]\mathrm{GPa}$. However, the fracture properties of spinel oxides grown at grain boundaries might differ from the values obtained for perfect spinels.

Experimentally, micro-cantilever bending tests have been used recently to assess the fracture energy and strength for bulk brittle materials and embrittled grain boundaries [44, 45, 46, 47]. Using this method, the fracture properties of Inconel 600 GB oxidized in PWR environment for different durations have been determined [47, 48, 49]. As intergranular oxides formed in Inconel 600 in PWR environment are also spinel type $(\mathrm{Fe}, \mathrm{Cr})_3\mathrm{O}_4$, the data reported in these experiments - $\gamma_c \in [1-4]\mathrm{J.m^{-2}}$ and $\sigma_c \in [350-1350]\mathrm{MPa}$ - might give first estimates on the intergranular oxide fracture properties for austenitic stainless steels. However, to the best of the authors' knowledge, there exists no experimental data for the fracture properties of austenitic stainless steel grain boundaries oxidized in PWR environment. The objective of this study is thus to perform micro-mechanical tests on micro-cantilevers containing austenitic stainless steel grain boundaries oxidized in PWR environment in order to assess their fracture properties.

The paper is organized as follows. In a first part, the material and experimental methods are described. This includes the description of the material, the oxidation experiments, the characterization of the oxides, the protocol to prepare the micro-cantilevers, the testing procedure as well the description of the theoretical framework and numerical simulations used to analyse the experiments. In a second part, the characterization of GBs after oxidation and the results of the micro-cantilever tests are described, as well as the results of the numerical simulations leading to an estimation of the fracture properties. In a third part, these properties are compared to the results available in the literature, as well as critically assessed with respect to their dependence to the experimental and numerical parameters.

2. Material and methods

2.1. Material description

The chemical composition of the material used in this study, denoted $FeCr_{12}Ni_{26}Si_3$ (wt %) in the following, is reported in the table 1. This composition has been chosen to emulate the enrichment of Ni and Si and depletion of Cr at grain boundaries in austenitic stainless steel 304 / 316 irradiated in PWR conditions [50] as a result of Radiation-Induced Segregation (RIS) [51]. This material can thus be considered as a model alloy - w.r.t. the chemical composition - for investigating the oxidation behavior and fracture properties of oxidized grain boundaries of moderate to highly irradiated austenitic stainless steels. Hence the results reported hereafter are expected to be relevant for the modeling of the IASCC phenomenon for the estimation of the GB resistance to cracking. The material chosen is not as suitable to reproduce the plasticity deformation mechanisms observed in irradiated materials, *i.e.*, strain localization, and thus could hardly be used to study the interaction between slip bands and grain boundaries often put forward to explain to increased cracking susceptibility due to irradiation. However, according to Schramm et al. [52] an enrichment in Si, as seen in the selected material, can lead to a decrease of the stacking fault energy, which results in an enhancement of planar slip and therefore promote the localization of the deformation.

Fe	**Cr**	**Ni**	**Mn**	**Si**	**Mo**	**C**	**Cu**
Bal	12	26	1.65	3	0.02	0.012	0.24

Table 1: Chemical composition of the alloy (main elements, wt %)

The material microstructure has been characterized through Electron BackScatter Diffraction (EBSD) (Fig. 1), showing mainly austenitic phase (FCC) with a very small amount (0.2%) of ferrite (BCC), in accordance with the prediction of Schaeffler's diagram owing to the Cr and Ni content. Using the `MTEX` toolbox [53], the average grain size has been estimated to about 11μm (Fig. 1a). The comparisons of the misorientation distribution to the McKenzie theoretical distribution (Fig.1b) shows that the material does not have significant crystallographic texture.

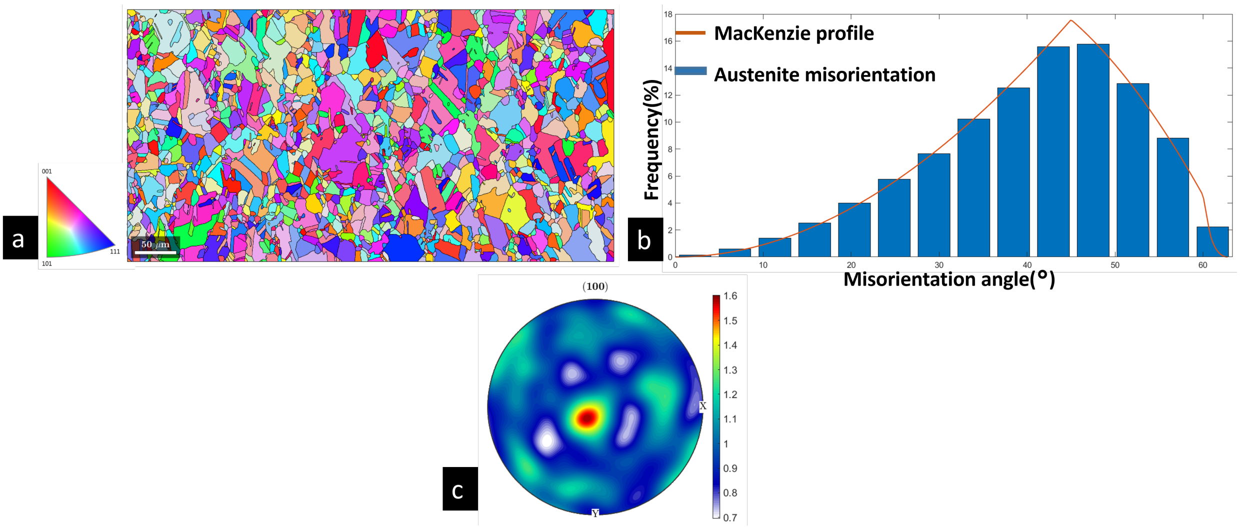

Figure 1: (a) EBSD inverse pole figure map [54] (b) distribution of the misorientation angle of the austenite phase and (c) Pole figure

The nature of grain boundaries is known to affect their oxidation behavior [22, 55], hence special grains boundaries are shown in Fig. 2. 44% of the total GBs length correspond to $\Sigma3$ grains boundaries which are almost immune to corrosion [55]. The distribution of GB misorientation thus presents a peak at 60°. Other special GBs are also present but in negligible amount.

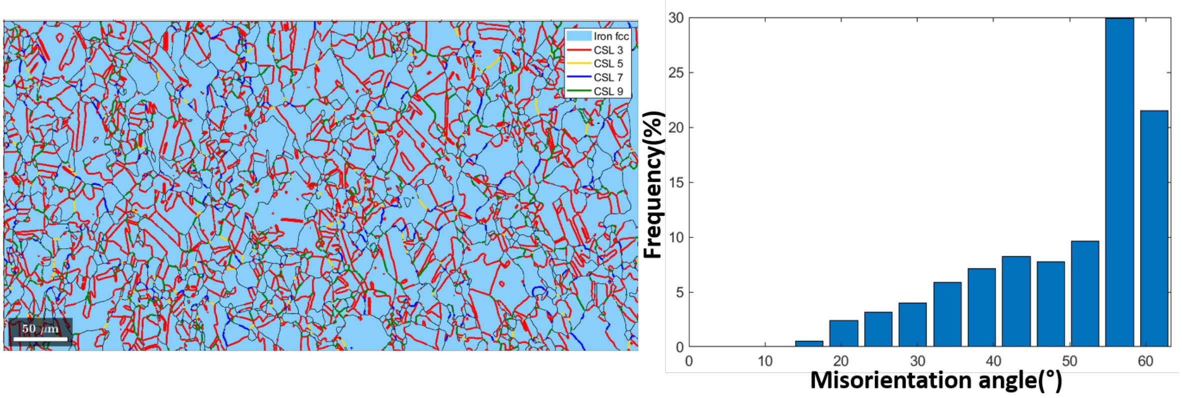

(a) (b)

Figure 2: (a) Special GBs identification and (b) distribution of GB misorientation angle

The conventional mechanical properties - yield stress YS, ultimate tensile strength UTS and uniform elongation UE - at 20°C and 350°C are reported in table 2. The material is harder than unirradiated solution annealed 304 / 316 austenitic stainless steels used for PWR internal structures, but with yield stress and ultimate tensile stress below the ones for which stress corrosion cracking is observed in cold-worked or irradiated austenitic stainless steels. In addition, Resonant UltraSound method (RUS) has been used to evaluate the Young's modulus Y_m and the Poisson's ratio ν_m at room temperature following the methodology detailed in [56].

Temperature (°C)	**YS** (MPa)	**UTS** (MPa)	**Elongation** %	$\boldsymbol{Y_m}$ (GPa)	$\boldsymbol{\nu_m}$
20	477 ± 5	645 ± 1	23 ± 2	188	0.31
350	370 ± 1	559 ± 11	20 ± 2	-	-

Table 2: Conventional mechanical properties at 20°C and 350°C: Yield strength YS, ultimate tensile strength UTS, uniform elongation UE, Young's modulus Y_m and Poisson's ratio ν_m of $FeCr_{12}Ni_{26}Si_3$

Tensile specimens of gage length 18mm × 2mm × 2mm and bars of dimensions 18mm × 2mm × 2mm have been extracted through electrospark machining from the $FeCr_{12}Ni_{26}Si_3$ plate. The surface of the samples have been grinded with SiC paper from 320 grade to 2400 then polished with diamond suspension from 3 to 1µm and finally vibro-polished 10h in OPS solution to eliminate the surface hardened zone induced by mechanical polishing.

2.2. Characterization of the IGSCC and oxidation behavior

The material is expected to be susceptible to IGSCC in PWR environment owing to its chemical composition. However, this susceptibility has to be assessed quantitatively. A Slow Strain Rate Tensile Test (SSRT) has been carried out on a tensile specimen in a 316L static autoclave equipped with a loading device. The simulated nominal PWR environment consists in deoxygenated high purity water with 25-35cc/kg H_2 STP, 1000ppm B and 2ppm Li at a temperature of 340°C and a pressure of 155 bars. A constant strain rate of $5.10^{-8}s^{-1}$ is applied to the sample. Stress-strain curve is recorded and the test is stopped when the plastic strain reached 4%, corresponding to 308h of testing. After the test, the sample surface is observed with a Scanning Electron Microscope (SEM) in secondary electron mode to detect and quantify intergranular cracking. As shown below, all grain boundaries are visible due to a different contrast with respect to the interior of the grains. Cracks appear with a darker contrast and are detected automatically based on a grayscale criterion.

In order to characterize the oxidation behavior through micro-cantilever beams, a bar sample has been oxidized in a 316L steel static autoclave using the same environmental conditions as for the SSRT test. Sample was hung with a wire in oxidized Zirconium to avoid galvanic coupling between the sample and the autoclave. A total oxidation time of 7470h was achieved with an interruption after 3680h where one-half of the bar was cut and removed for characterization. After oxidation, the surface of both samples are first observed with SEM. In order to quantify the oxides dimensions, Focus Ion Beam (FIB) is used to polish a 200μm deep cross-sectional region on the samples, allowing to measure with SEM the thicknesses of the inner and outer oxide layers as well as the depth and width of oxide penetration at grain boundaries, as a function of oxidation time. As shown below, oxidation is not homogeneous, thus several measurements are made along the 200μm length and average and maximum / minimum values are reported. In order to quantify the chemical composition of the different oxide layers, a Transmission Electron Microscope (TEM) lamella located perpendicular to the sample surface at a grain boundary has been extracted on the 7470h oxidized sample using FIB lift-out technique. Analysis has been performed using a TEM Tecnai F20^2 equipped with a Energy Dispersive Spectroscopy (EDS) detector.

2.3. Characterization of oxidized grain boundaries fracture properties

The fracture properties of oxidized grain boundaries are obtained using micro-cantilever beam bending experiments. The preparation of micro-cantilever, test conditions, post-test characterizations and analysis are detailed in this section.

2.3.1. Micro-cantilevers milling and testing

FIB cross-sectional polishing (Fig. 3a) is carried out at 30 kV with currents from 47nA down to 2.5 nA to mill a 150μm × 5μm × 18μm trench in order to remove the oxide layer on the side of the sample. This operation allows performing an EBSD map (Fig. 3b) to get the crystallographic orientations of the grains and the position of grain boundaries. Locations where micro-cantilever beams can be milled are chosen with the following requirements: in large grains (10 to 15μm), including a grain boundary mostly perpendicular and close to the surface. One example of such location is shown in Fig. 3c.

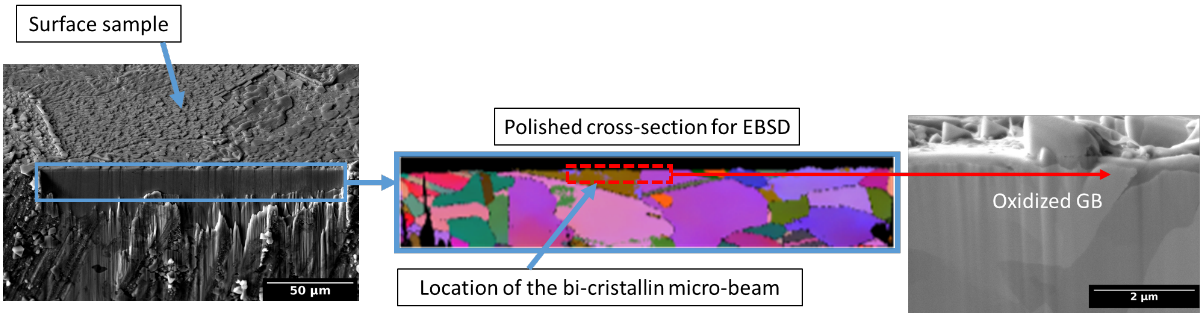

(a) (b) (c)

Figure 3: (a) FIB cross-sectional polishing [54] (b) EBSD mapping [54] and (c) selection of the location of the micro-cantilever beam

The fabrication of micro-cantilevers containing a single grain boundary is shown in Fig. 4. Trenches are milled on the sides (17μm × 5μm × 18μm) and in front (5μm × 5μm × 18μm) of the micro-cantilevers using current from 21nA down to 2.5nA. After a 180° rotation of the sample, a 17μm × 8μm × 10μm trench is milled under the micro-cantilever to cut the bottom from the bulk using currents from 21nA down to 0.78nA. A final polishing of the micro-cantilever sides is realized at 0.78nA to obtain the final shape and surface finish.

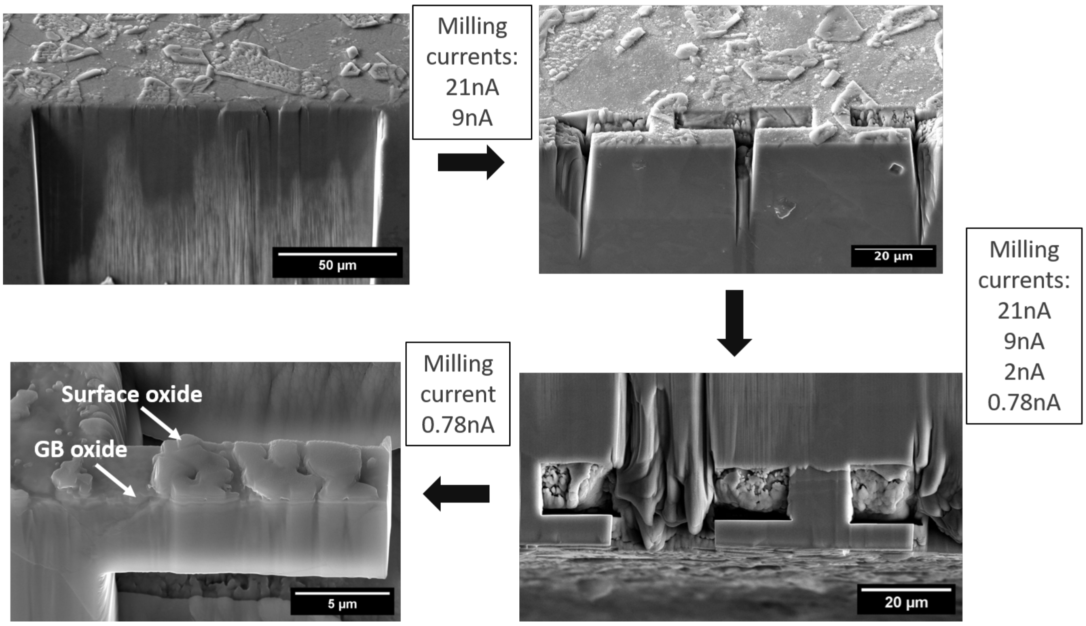

Figure 4: Milling protocol of the micro-cantilever beams

This protocol leads to bi-crystalline micro-cantilever beams with an oxidized grain boundary close to the clamped end. These beams are characterized by their dimensions (about 15μm × 5μm × 5μm), crystallographic orientations of both grains, thickness of the inner and outer oxides, and depth and width of the intergranular oxide penetration. All these characteristics are reported in the results section. It should be noted that, except for the overall dimensions, all measurements are performed only on one side of the beams. Given the mean grain size, the choice of large grains and the typical width of the beams, it is however expected that there is a single grain along the width. On some samples, the heterogeneous external oxide layer has been removed (Fig. 5) in order to assess its potential effect on the measured fracture properties.

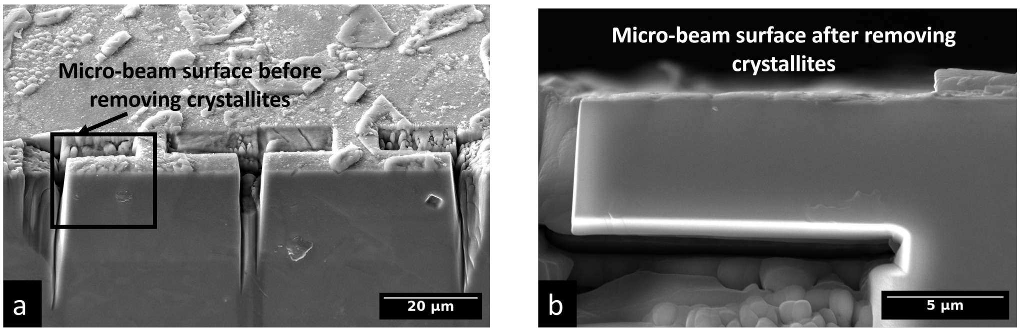

Figure 5: (a) Milling of the micro-beam: presence of surface crystallites (b) Surface of the micro-beam after crystallites removal

Bending tests are carried out on the micro-cantilever beams in a HeliosNanoLab600i FIB/SEM (FEI) at room temperature using a FT-NMT-04 (FemtoTools) micro-testing device in displacement-control mode. The free end of the cantilever is loaded using a Berkovich indenter tip at a displacement rate of 20nm.s^{-1} (Fig. 6a) up to the fracture of the grain boundary and / or significant plasticity. Load-displacement curve is recorded. Due to the high axial rigidity of the device, it has been checked that the displacement measured by the testing device corresponds to the displacement of the beam at the loading point, hence no correction of the displacement is made in the following. The use of a Berkovich indenter allows to precisely mark the loading point, facilitating the measure of the distance from the loading point to the clamped end, which is needed for further analysis. No deep indentation of the beam by the Berkovich tip was observed after the tests, allowing us to use the displacement values without correction. As shown in Fig. 6a, in-situ experiments and locating the micro-cantilever beams on the edge of the samples allow to correlate load-displacement curves to microscopic events.

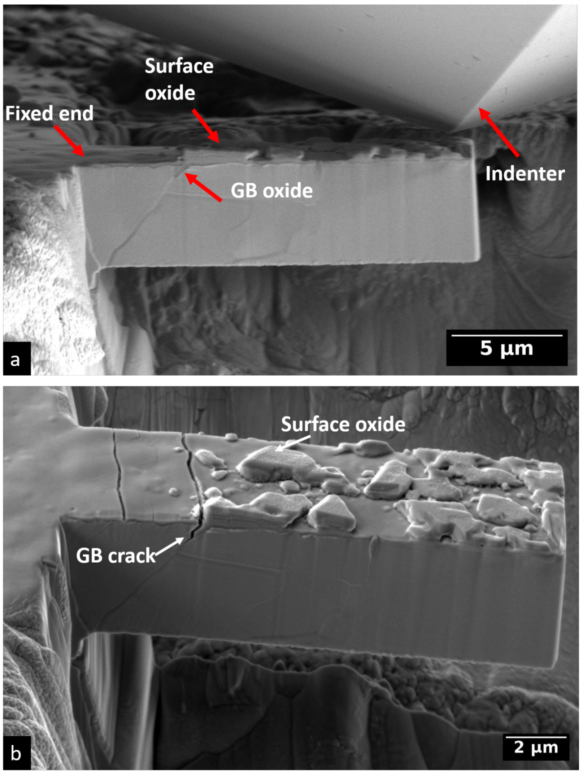

Figure 6: SEM observation (a) at the beginning and (b) at the end of the bending test on the micro-cantilever beam

2.3.2. *Post-test characterization*

After the tests, SEM observations of the micro-cantilever beams are performed on the top surface and the side surface not visible during the tests (Fig. 6b) in order to visualize cracks and to estimate fracture surface. Two different methods are used. For all tests, an estimate of the fracture surface is obtained by measuring the crack depths on both sides of the micro-cantilever beam as well as the crack trace on the top surface, and assuming a linear variation of the (planar) crack front along the width. As this estimation relies on rather strong assumptions, another technique, referred to as 3D tomography in the following, has been used for some beams. FIB along with the Slice&View software is used to remove a slice on the side of the micro-beam using the ion Ga^+ beam at 0.23nA followed by a picture with the electron imaging system (Fig. 7). The sequence is repeated until all the beam volume has been removed. The slice width is chosen between 50 and 100nm, leading to a set of 50 to 490 pictures depending on beams. Fiji and Matlab softwares are then used to evaluate the fracture surface based on the Delaunay triangulation of the crack coordinates. In addition, the ORS Dragonfly software [57] has also been used to visualize the crack volume within the micro-beam.

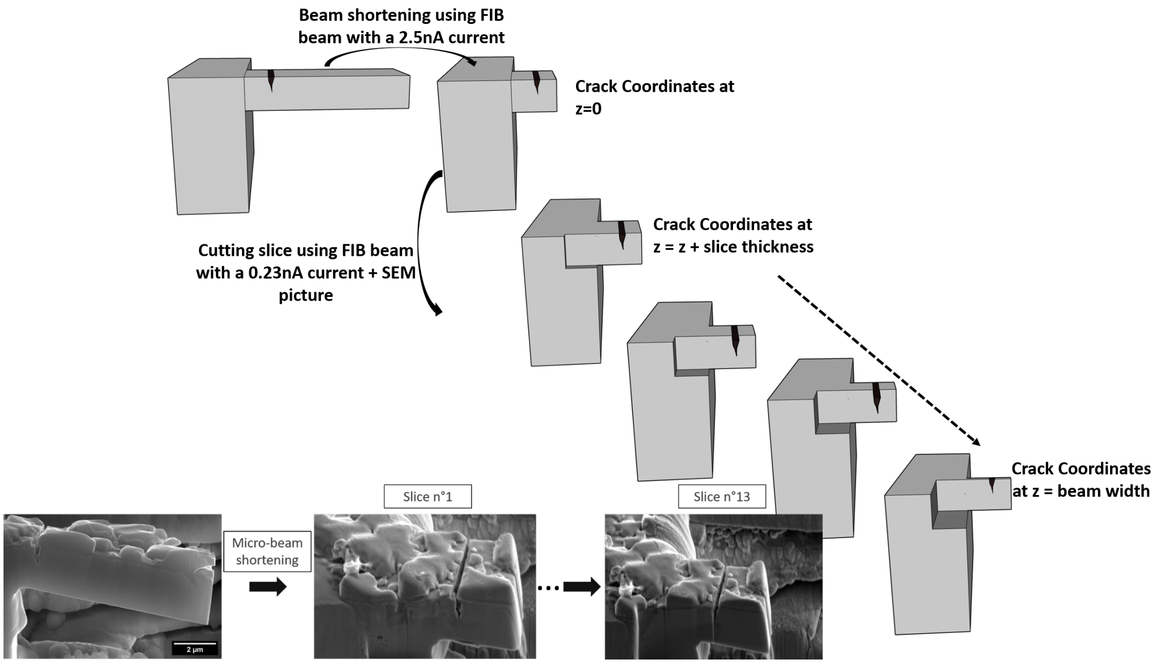

Figure 7: 3D tomography protocol used to evaluate fracture surfaces

2.3.3. Analysis of the experiments

Two kinds of micro-cantilever beam tests are performed in the literature, depending on the presence of an initial crack / notch or not. In the former case, crack propagation is assessed, and the associated mechanical quantity is the fracture toughness / fracture energy [58]. In the latter case, which is the one considered in this study, crack initiation is investigated. The Coupled Criterion (CC) [59] has been shown to lead to prediction of crack initiation in brittle materials in agreement with experimental observations. According to this model, cracking initiation over a surface S_c occurs when both a stress and energy criteria are satisfied. The stress criterion states that the stress σ should be higher or equal to the strength of the material σ_c which is the first material fracture property:

$$\sigma\left(x \in S_c\right) \geq \sigma_c \tag{1}$$

The energy criterion is the same as Griffith's criterion and states that the variation of elastic energy in the system due to cracking $\Delta\mathcal{E}$ (counted positively) should be higher than the fracture energy:

$$\Delta\mathcal{E}_{el} \geq \gamma_c S_c \tag{2}$$

where γ_c is the surface fracture energy, the second material fracture property. For a particular experiment, satisfying Eq. 1 and Eq. 2 allows finding both the macroscopic load for crack initiation and the crack size. In the presence of a pre-existing crack, the stress criterion (Eq. 1) is satisfied at the crack tip due to the stress singularity, and the coupled criterion tends towards the Griffith's criterion. While the coupled criterion has been shown to lead to good predictions with respect to experimental observations, Eqs. 1, 2 shows that estimating the fracture properties is not straightforward. First, only upper-bounds of σ_c and γ_c can be obtained in general due to the presence of inequalities in Eqs. 1, 2. Second, the relevant stress value in Eq. 1 is a matter of question. Third, as crack initiation over a finite size (thus satisfying Eq. 1) can be followed by crack propagation (where Eq. 1 is automatically satisfied due to the stress singularity), applying Eq. 1 is in fact not as simple as it may seem. This theory is used in the following to analyze each experiment separately by assuming that (1) the relevant stress in Eq. 1 is the maximal principal stress in the intergranular oxide, (2) Eqs. 1, 2 are equalities, but keeping in mind that then the values obtained for σ_c and γ_c are upper-bounds.

As shown in the results section, Eq. 2 can be applied directly using the load-displacement curves to compute the release of elastic energy associated with cracking. However, a model is required to estimate the stresses in the beam to apply Eq. 1. One way consists in using elastic beam theory that gives the relation between the applied load / displacement and the geometrical parameters characterizing the beam and the local stresses. However, this method suffers from various drawbacks: elastic beam theory relies on the assumption of homogeneity of the material and large slenderness ratio. These two assumptions are not valid for the beam considered due the the presence of two grains and the oxide layer as well as rather short beams w.r.t. the thickness. Hence, this method leads to crude estimates of local stresses. Therefore, Finite Element simulations have been performed to compute local stresses. For each micro-cantilever beam, a mesh composed of linear elements is constructed using the geometrical parameters measured experimentally, *i.e.*, overall dimensions of the beam, presence of the two grains, of the oxide layer and of the intergranular oxide penetration and inclination of the grain boundary. A typical finite element mesh is shown in Fig. 8. The dimensions of the support to which the beam is attached and the mesh density have been selected to ensure that they do not affect the results.

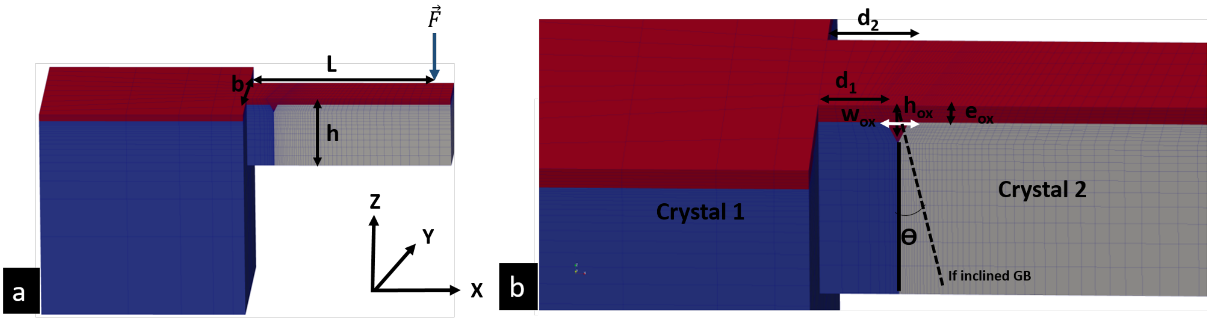

Figure 8: Typical mesh of a micro-cantilever beam where the different colors correspond to the grains (white / blue) and the oxide red)

Lateral and bottom surface of the support are clamped, and a force is applied at the loading point. The materials (grains, oxide) are assumed to follow Hooke's law, with cubic elasticity for the FCC grains and isotropic elasticity for the oxide. Cubic elasticity requires three input parameters, C_{11}, C_{12} and C_{44} that fully define the stiffness tensor [60]. These parameters are obtained from the polycrystalline elasticity moduli Y_m and ν_m (Table 2) using (1) the Hershey-Kröner-Eshelby model to relate C_{ij} to the shear modulus $\mu_m = Y_m/[2(1+\nu_m)]$ [61], (2) a constant bulk modulus at the polycrystalline and single crystal scale $K_m = Y_m/[3(1-2\nu_m] = [C_{11}^m + 2C_{12}^m]/3$ and (3) assuming that the Zener ratio $Z = 2C_{44}^m/[C_{11}^m - C_{12}^m]$ is equal to $Z = 3.5$ [61]. Solving these equations leads to the following elastic constants C_{11}^m=209GPa, C_{12}^m=143GPa and C_{44}^m=116GPa. Assuming that the (inner) oxide is polycrystalline and isotropic at the scale considered, the corresponding Young's modulus Y_{ox} and Poisson ratio ν_{ox} are computed as follows. Crystal scale cubic elastic parameters for $FeCr_2O_4$ (resp. $NiCr_2O_4$) spinels have been estimated from Molecular Dynamics simulations at room temperature, leading to C_{11}^{ox}=272GPa (resp. C_{11}^{ox}=287GPa), C_{12}^{ox}=130GPa (resp. C_{12}^{ox}=190GPa) and C_{44}^{ox}=94GPa (resp. C_{44}^{ox}=86GPa) [62]. The corresponding bulk and shear moduli at the polycrystalline scale can then be computed using the equations detailed hereabove, allowing to obtain $Y_{ox} = 218$GPa / $\nu_{ox} = 0.29$ for $FeCr_2O_4$, and $Y_{ox} = 187$GPa / $\nu_{ox} = 0.36$ for $NiCr_2O_4$. As detailed in the results, the inner oxide layer chemical composition is more complex than these two limiting cases, but the ratio of Fe over Ni is close to 1. Hence, in the following, average values are used: $Y_{ox} = 202$MPa / $\nu_{ox} = 0.32$. All simulations have been performed using the `Cast3M` 2022 finite element solver [63] under small strain assumption. For a given applied load, the maximal and minimal largest principal stress σ_I in the intergranular oxide are extracted from the simulation to use Eq. 1. Note finally that these simulations require the crystallographic orientations of the grains as input parameters. For some cases, this information was not available. Hence, isotropic elasticity was assumed for the grains with the same moduli as for the oxide. This allows accounting for the effect of beam geometry on the local stresses, but not for the elastic mismatch between the grains and the oxide.

The previous type of simulations aims at estimating the local stresses in the micro-cantilever beams. A second type of simulations is also used in this study, similar to the previous one but adding Cohesive Zone Model (CZM) elements inside the intergranular oxide. More precisely, CZM elements are added on the plane where the GB initially lies. These 2D elements relies on a traction-separation law that link the normal t_n and tangential t_t stresses to the normal Δu_n and tangential Δu_t displacement jumps. Tvergaard model is used in the following [64]:

$$t_n = \begin{cases} \frac{27}{4}\sigma_c \frac{\Delta u_n}{\delta} \max\left(1 - \frac{\Delta u_n}{\delta}, 0\right)^2 & \text{if } \Delta u_n \geq 0 \\ k\Delta u_n & \text{otherwise} \end{cases} \qquad t_t = k\Delta u_t \tag{3}$$

that aims at modelling cracking. This model requires two parameters, the strength σ_c and the critical opening δ or alternatively the fracture energy $\gamma_c = [9/16]\sigma_c\delta$. Thus, the fracture parameters obtained with the previous type of simulations can be used as input data to assess their capacity to predict the cracking. The stiffness k is set to a value high enough to have no effect on the results, $k = 10^{11}\text{MPa.m}^{-1}$. More advanced models have been proposed in the literature accounting for shear failure, at the expense of additional parameters [65]. Here the simplest model is used to assess the two main fracture properties, but its use is restricted to situations where mode I failure prevails. Note finally that contrary to bilinear models widely used in the literature [65], the stiffness of the CZM element in opening mode ($\Delta u_n > 0$)) depends on the fracture parameters. However, the range of values of σ_c and δ used in the following leads to stiffness high enough to have a negligible effect on most simulations. Simulations are performed to predict the load-displacement curves, including cracking if any. As CZM may lead to snap-back events, thus compromising convergence of the numerical algorithm, a path-following technique available in `Cast3M` 2022 is used: a constant increase of the opening of the CZM element at the free surface is prescribed, and the displacement at the loading point is found as a result.

3. Results

3.1. Intergranular cracking susceptibility and oxidation behavior

SEM observations of the tensile specimen surface after the SSRT test in PWR environment is shown in Fig. 9. A homogeneous oxide layer has been formed on the sample with almost no visible crystallite. The grain boundaries exhibit a distinctive contrast from the interior of the grains, indicating a difference in the oxide layer. Observations at higher magnification show that the highest contrast corresponds to intergranular cracks, allowing to set a grayscale threshold above which cracks are detected. Crack density is estimated to be about 300mm^{-2} with a mean crack length of 25μm (for a mean grain size that has been evaluated to 11μm). These values can be compared to the typical values obtained for irradiated austenitic stainless steels tested in PWR environment. Crack densities of about 300mm^{-2} have been reported in [66] for various irradiation conditions of a SA304L steel SSRT tested to 4% plastic strain, with mean crack size of about 17μm, for a grain size of about 21μm. For similar conditions and material, lower crack densities have been reported in [67]. Clearly, the evaluation of crack densities from surface observations depends on the detection method used, but qualitative conclusions can nevertheless be drawn from the previous results. $\text{FeCr}_{12}\text{Ni}_{26}\text{Si}_3$ alloy is susceptible to IGSCC in PWR environment, with a susceptibility - as measured through crack densities and relative crack size (*w.r.t.* to the grain size) for a given strain - on the same order or higher than the one of irradiated 304 steel. This observation confirms the effect of the local chemical composition observed in irradiated 304 / 316 GB on the IGSCC susceptibility.

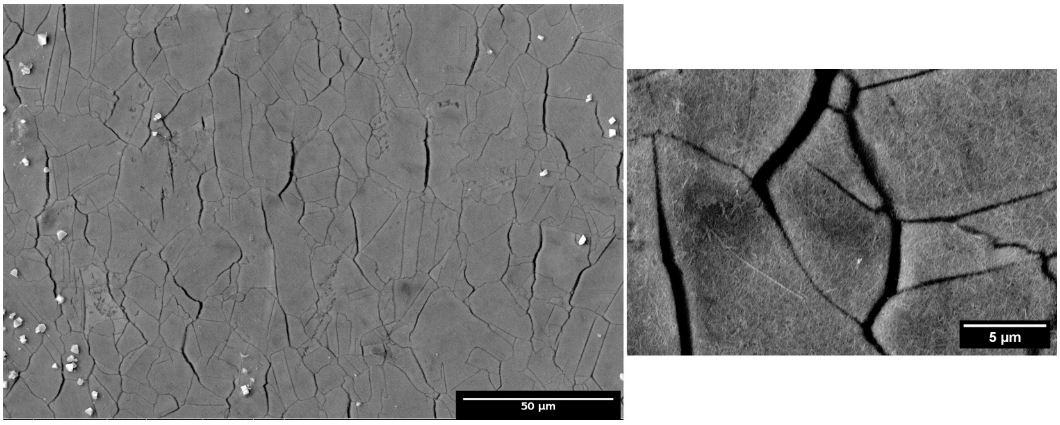

Figure 9: SEM observations of the tensile specimen surface after SSRT test in PWR environment

SSRT test corresponds to rather short oxidation time (308h). SEM observations of the surface of bars oxidized for 3680h and 7470h are shown in Fig. 10. Contrary to what has been observed in Fig. 9, the oxide layer is very heterogeneous, with presence of large crystallites. Fig. 10b shows a strong dependence of the oxide growth to the underlying microstructure, as the different grains can almost be detected from these images. These observations are different from the ones obtained on 304 / 316 stainless steel [68] for similar oxidation time, but closer to what is observed on Nickel-based alloys.

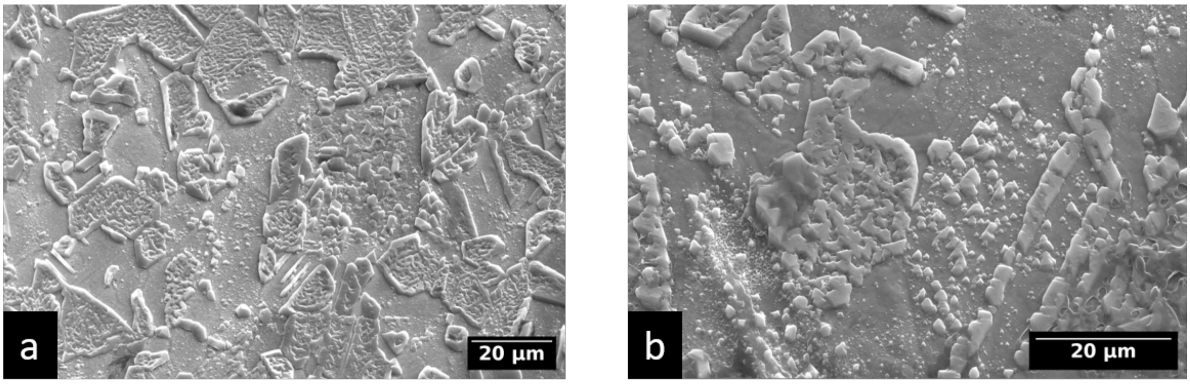

Figure 10: Typical SEM observations of the bar surfaces after (a) 3680h and (b) 7470h oxidation in PWR environment [54]

Typical SEM observations on the bars cross-section are shown in Fig. 11. These observations first confirm the heterogeneous nature of the outer oxide layer observed from the surface, with presence (Fig. 11a) or absence (Fig. 11b) of crystallites. Second, a continuous oxide layer - denoted as inner oxide layer in the following - is observed. This layer is more homogeneous, but still presents significant thickness variations. Third, preferential oxidation is observed at grain boundaries, with intergranular oxide penetration up to about 1μm. Again, significant variations are observed from one grain boundary to another, as shown in Fig. 11.

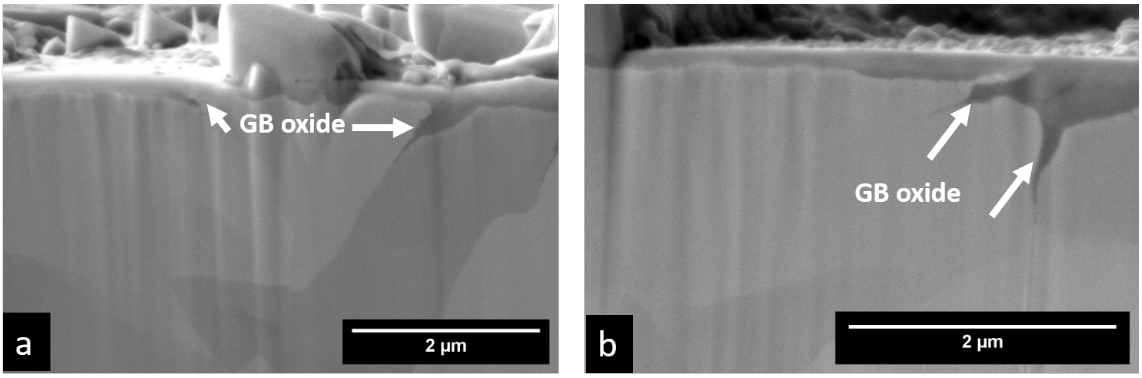

Figure 11: Typical SEM observations of the bars cross section after (a) 3680h and (b) 7470h oxidation in PWR environment

The SEM observations of the oxide layers show an important surface and intergranular oxidation. The geometrical properties of the oxide layer formed after 3680h and 7470h are reported in Tab. 3 according to the methodology described in Section 2.2. No significant difference of the oxide layer is observed as a function of oxidation time. Hence both samples are not distinguished in the following. Compared to 304 / 316 austenitic stainless steels, the inner oxide thickness and intergranular oxide depth are larger than what is usually reported at 340°C - which is the relevant temperature for PWR internals structures - but somewhat closer to observations made at 290°C [40]. This is in agreement with the results available in the literature regarding the effect of Cr, Ni and Si content on oxidation behavior of austenitic stainless steels in PWR environment [69].

Oxidation duration	**Crystallites height (μm)**	**Inner oxide thickness (nm)**	**Intergranular oxide depth (μm)**	**Intergranular oxide width (μm)**
3680h	0.6 ± 0.1	113 ± 65	1.0 ± 0.2	0.5 ± 0.1
7470h	0.9 ± 0.2	123 ± 19	1.2 ± 0.2	0.6 ± 0.2

Table 3: Geometrical properties of oxides formed on the $FeCr_{12}Ni_{26}Si_3$ steel oxidized 3680h and 7470h in PWR environment

The oxides chemical composition has been analyzed using TEM-EDS for the surface and GB oxides. EDS maps of the main chemical elements are shown in Fig. 12. Several observations can be made from these measurements. The crystallites are mainly composed of Fe and O, and to a lesser extent of Ni. These crystallites are not in contact directly with the underlying material but with an inner oxide layer enriched in Cr and Si. The intergranular oxide has the same composition and can thus be considered as part of the inner layer. Other elements such as Ca (and to a lesser extent Zn) have also been detected in significant amount in the inner oxide layer.

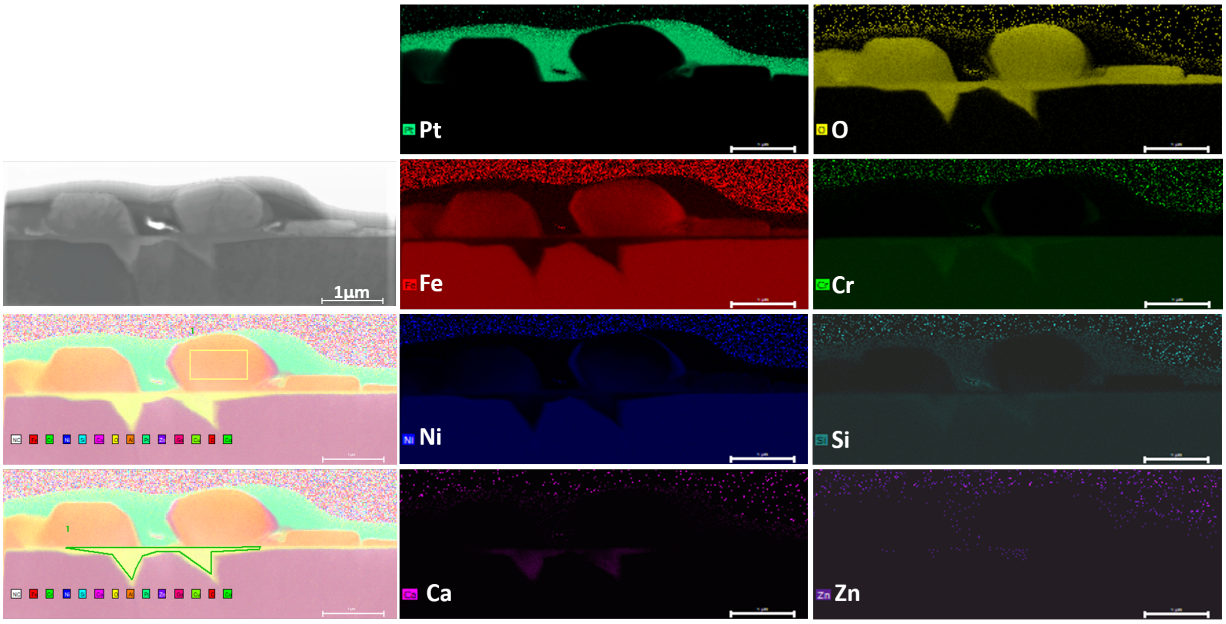

Figure 12: TEM-EDS elemental mapping of a cross-section of a bar after 7470h in PWR environment. Pt corresponds to the layer deposited on the sample surface before the FIB processing of the TEM foil. Regions delimited by yellow and green curves are used to determine the outer and inner layer composition, respectively.

The composition of the surface crystallite / outer layer and the inner oxide layer, averaged over the areas shown in Fig. 12, are reported in Tab. 4. The analysis leads to global compositions of $(Ni_{0.9}, Fe_{1.6})Fe_2O_4$ for the outer oxide and $(Ni_{0.7}Si_{0.5}Ca_{0.2}Zn_{0.2})(FeCr)O_4$ for the inner oxide. These oxide compositions are more complex than those commonly encountered on 304 / 316 austenitic stainless steels. On the one hand, the outer oxide composition is close to the magnetite Fe_3O_4 often reported in the literature. On the other hand, the inner oxide composition differs significantly to the $(Ni_x, Fe_{1-x})Cr_2O_4$ spinel oxides. The presence of Ca and Zn, whose origin is still under investigation, complicates the comparison of the inner oxide to other data from the literature.

	O	**Fe**	**Cr**	**Ni**	**Si**	**Ca**	**Zn**	**Al**
Crystallite	46	42	0.2	10	0.4	0	0.6	0.8
Inner oxide	51	15	14.5	8	6	3	2	0.5

Table 4: Oxides compositions (at %) measured on the TEM foil shown in Fig. 12

The results presented in this section regarding the intergranular cracking susceptibility and the oxidation behavior of the $FeCr_{12}Ni_{26}Si_3$ alloy lead to the following conclusions. The material, chosen as a model alloy regarding the effect of irradiation on 304 / 316 steel on GB local chemistry, is indeed both susceptible to intergranular oxidation and to IGSCC in PWR environment. The chemical composition of the intergranular oxides differs however from the ones usually reported for 304 / 316 steels. In the next section, the fracture properties of these intergranular oxides are assessed with the micro-cantilever beams bending tests.

3.2. Mechanical tests

Fig. 13 shows the load displacement curves for all micro-cantilever beams tested in this study. A linear elastic regime is observed for each test, followed for some of them by a non-linear plasticity regime. For 12 out of 16 tests, a load drop can be seen in the elastic regime or early in the plastic regime that corresponds to the initiation and propagation of a crack in the intergranular oxide visible in SEM side images. In some cases, multiple load drops can be observed, as for Micro-beam1-ox7470h and Micro-beam2-ox7470h in Fig. 13b, that corresponds to multiple cracking of the outer oxide layer outside the oxidized grain boundary. A significant scatter regarding failure load and elastic slope is also observed coming mainly from the differences of beam dimensions as shown in the simulations, and to a lesser extent to differences of the crystallographic orientations of the grains and of the thickness of the oxide layer.

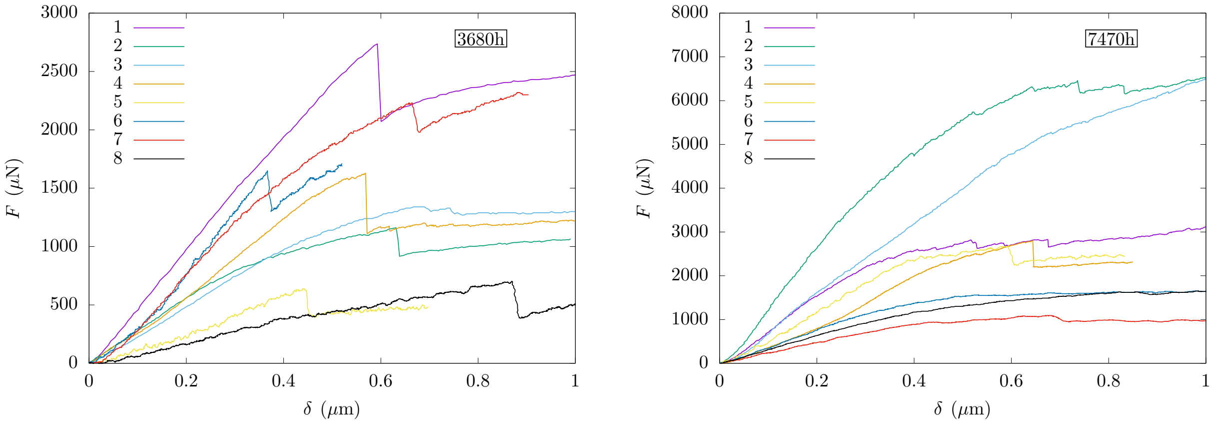

(a)

(b)

Figure 13: Load - Displacement curves from the micro-cantilever beam bending experiments: (a) 3680h and (b) 7470h oxidized samples data

The two typical load displacement curves are presented in Fig. 14 where cracking occurs in the elastic regime (Fig. 14a) or after early stage of plastic deformation (Fig. 14b). Critical forces just before and after cracking denoted F_c^1 and F_c^2, respectively, are extracted for each test. The associated displacement δ_c is also extracted. In absence of significant plasticity, δ_c is simply the displacement for which cracking occurs. Otherwise, δ_c is defined as the elastic part of the displacement (Fig. 14b). As detailed below, this allows to compute the release of elastic energy due to cracking.

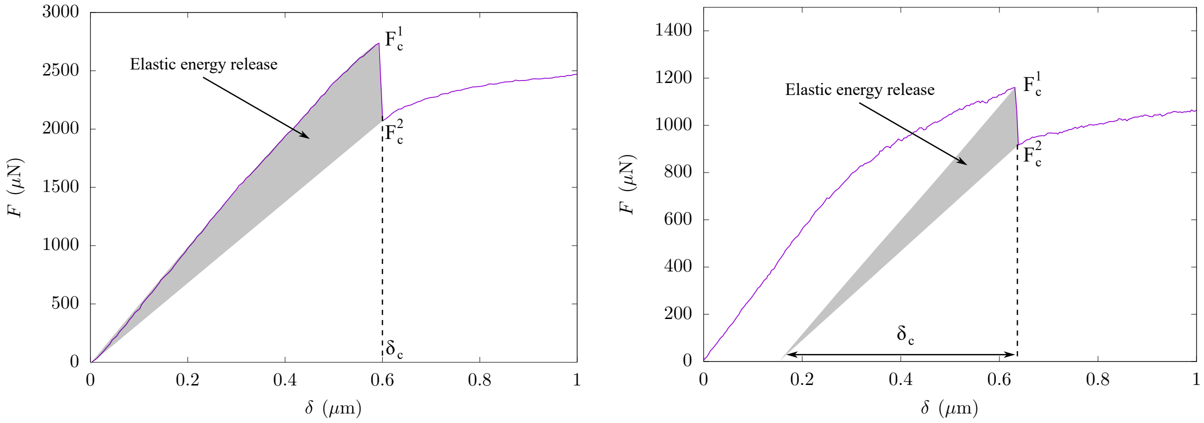

(a) (b)

Figure 14: Typical Load - Displacement curves from the micro-cantilever testing with intergranular fracture allowing to obtain load before F_c^1 and after F_c^2 failure and the elastic displacement at failure δ_c (a) in absence or (b) in presence of plasticity. The associated elastic energy release corresponds to the shaded areas.

Typical SEM observation of a beam after testing is shown in Fig. 15a. A main crack is observed at the oxidized grain boundary, that can be located either at the metal / oxide interface (7/12, Fig. 15b) or within the intergranular oxide (5/12, Fig. 15c). For all tests leading to fracture, the intergranular crack initiates and propagates at the load drop on a length equal to the depth of the intergranular oxide, and do not propagate further upon additional loading. Additional cracks may also be observed on the outer oxide layer, as shown in Fig. 15a. The depths of the intergranular crack on both side of the beam have been measured in order to compute a first estimate of the fracture surface, as described in Section 2.3.2.

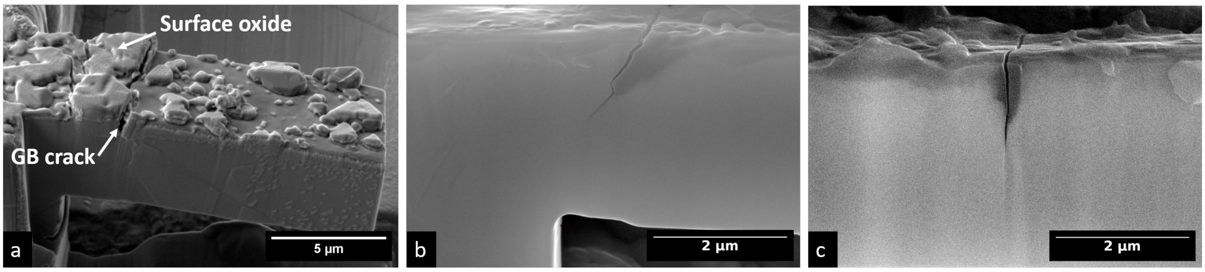

Figure 15: (a) Typical SEM observations of a micro-beam with a GB crack after the bending test. Cracks may be (b) at the interface between the metal and the oxide or (c) within the intergranular oxide

For 5 out of 12 beams, 3D tomography has been used to estimate the crack surface. In all cases, the crack surface measured by tomography is greater that the one estimated by measuring the depth of the crack on each side of the beam and assuming a linear variation of the crack front along the width. For Micro-beam4-ox7470h, the difference between the two techniques is minor ($15\mu\text{m}^2$ *vs.* $15.4\mu\text{m}^2$), but in other case like Micro-beam5-ox3680h, the cracking surface measured by tomography is three times larger. Fig. 16 shows the 3D reconstruction of the crack path for one of these beams. The crack path appears to be tortuous, also exhibiting branching, explaining the differences than can be observed between the simple estimate of crack surface and 3D tomography measurements. In the following, crack surfaces reported correspond to 3D tomography if the measurement was performed. Otherwise, the simple estimate is used.

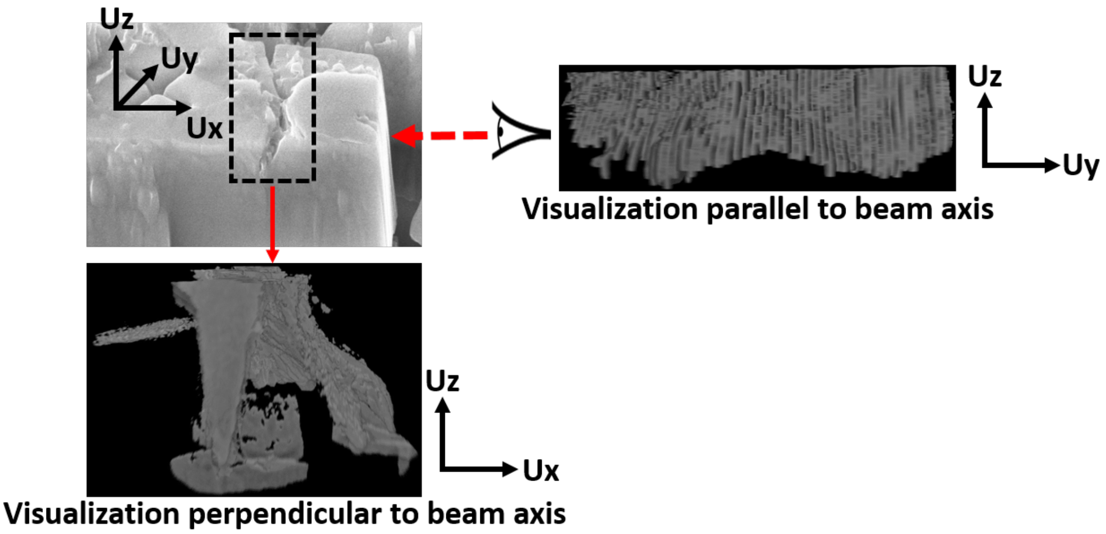

Figure 16: 3D visualization of the volume morphology of the crack path

The main data pertaining to crack initiation and defined in Figs. 8 and 14 are summarized in Tab. 5. Other data relevant to perform the simulations reported in the following are given in Appendix A.

	Length (L) (μm)	**Width (b)** (μm)	**Height (h)** (μm)	$\boldsymbol{h_{ox}}$ (μm)	$\boldsymbol{F_c^1}$ (μN)	$\boldsymbol{F_c^2}$ (μN)	$\boldsymbol{\delta_c}$ (μm)	$\boldsymbol{S_c}$ (μm^2)
Micro-beam1-ox3680h**	14.5	6.3	6.0	0.94	2750	2066	0.60	13.0*
Micro-beam2-ox3680h	16.2	5.3	4.7	0.92	1239	985	0.50	6.8
Micro-beam3-ox3680h	14.0	5.8	3.7	0.48	1300	1200	0.52	4.2
Micro-beam4-ox3680h	11.2	5.3	4.3	0.84	1626	1105	0.51	9.2
Micro-beam5-ox3680h**	8.4	3.8	2.0	1.08	620	405	0.44	9.1*
Micro-beam6-ox3680h	11.5	3.4	4.0	1.30	1650	1300	0.37	5.8
Micro-beam7-ox3680h	12.8	4.1	5.4	0.98	2240	1970	0.59	6.0
Micro-beam8-ox3680h**	12.3	3.6	2.9	1.19	725	430	0.89	10.0*
Micro-beam4-ox7470h**	12.0	5.0	5.1	1.15	2790	2210	0.53	15.4*
Micro-beam5-ox7470h**	12.9	5.8	5.0	1.02	2630	2270	0.41	16.5*
Micro-beam6-ox7470h**	15.3	5.0	5.0	0.36	1550	1526	0.42	2.0
Micro-beam8-ox7470h**	14.7	5.0	4.9	1.34	1646	1540	0.55	7.0

Table 5: Main geometrical parameters and results of the micro-cantilever bending tests. Data marked by ** differentiate failure at the metal / oxide interface from failure within the intergranular the oxide. Fracture surface marked by * have been measured with 3D tomography.

3.3. Estimation of fracture properties

These experimental data are now used to estimate the fracture properties. The elastic energy release due to cracking can be computed as:

$$\Delta\mathcal{E}_{el} = \frac{(F_c^1 - F_c^2)\delta_c}{2} \tag{4}$$

which corresponds to the shaded areas in Fig. 14. Eq. 4 is used as an estimate of the fracture energy γ_c through Eq. 2, leading to the results shown in Fig. 17a. The estimated fracture energy ranges from 2J.m^{-2} to 15J.m^{-2}, which is in the range of theoretical and numerical data reported in the literature for $(\mathrm{Fe, Ni})\mathrm{Cr_2O_4}$ spinel [42, 43], as discussed in the introduction. The average value for metal / oxide fracture (8J.m^{-2}) is slightly lower that for oxide fracture (11J.m^{-2}). However, the elastic energy release per unit cracking surface $\Delta\mathcal{E}_{el}/S_c$ is only a crude estimate of the real fracture energy for various reasons. First, from a theoretical point of view, it is only an upper bound of γ_c according to Eq. 2. Secondly, fracture surface measurements have been performed at the end of the tests, *i.e.*, with significant deformation post fracture (Fig. 13). It is thus possible that the fracture surface areas measured are an upper bound of real fracture surface that corresponds to the load drops. Thirdly, the measurement of the cracking surface suffers from large uncertainties as shown in the previous section. Even restricting to beams where 3D tomography has been performed, all corresponding to metal / oxide fracture, the fracture energy estimates ranges from 4J.m^{-2} to 15J.m^{-2} (Fig. 17a). All together, it is difficult to extract a lower bound or an upper bound of the fracture energy from Fig. 17a, and the average values estimated for metal / oxide (8J.m^{-2}) and oxide (11J.m^{-2}) fracture are considered in the following.

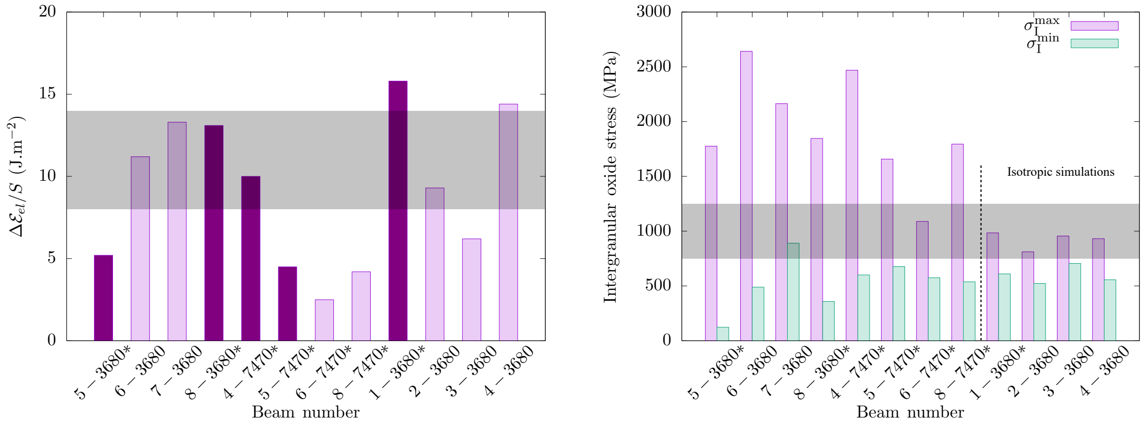

(a)

(b)

Figure 17: (a) Elastic energy release computed with Eq. 4 per unit cracking surface S_c. Darker color corresponds to beams where 3D tomography was used to evaluate S_c (b) Maximal and minimal largest principal stress σ_I in the intergranular oxide computed with FE simulations for an applied load equal to F_c^1. Shaded areas corresponds to ranges used in CZM simulations.

Fig. 17b shows the maximal and minimal largest principal stress, σ_I^{max} and σ_I^{min}, in the intergranular oxide computed with FE simulations for an applied load equal to F_c^1, *i.e.*, just prior to failure. For σ_I^{max}, values lies between about 900MPa to about 2600MPa. Values computed assuming an isotropic behavior, for cases where the crystallographic orientations of the grains were not available, are significantly lower, showing the strong effect of both the anisotropy of the grains and the elastic mismatch between the oxide and the grains on local stresses. This point will be further discussed in Section 4. In the following, these data are not used. According to Eq. 1, the oxide strength is such that:

$$\sigma_c \leq \min \sigma_I^{max} \tag{5}$$

to ensure that the stress criterion is satisfied for all beams at initiation, leading to a value of σ_c of about 1000MPa. The values of σ_I^{min} are less easy to analyse. According to the coupled criterion, Eq. 1 should apply on the whole crack path. However, this is only true in the initiation phase. The data obtained for Micro-beam5-3680h where σ_I^{min} is close to zero, *i.e.*, the intergranular oxide extends down to the neutral axis of the beam, show that crack initiation is followed by crack propagation, at least for some beams tested in this study. Hence only Eq. 5 is considered for the estimation of σ_c.

The analysis of Fig. 17 according to Eqs. 1 and 2 thus leads to an estimate of the fracture energy $\gamma_c \approx 11$J.m^{-2} (for the oxide) and a strength $\sigma_c \approx 1000$MPa. It can be noted that these values are similar between the micro-beams from the 3680h sample, with large surface crystallites, and the micro-beams from the 7470h sample which have their surface crystallites removed, showing the negligible effect the outer layer has on the results. In order to refine these estimates and to assess their ability to lead to quantitative predictions, FE simulations with CZM have been performed considering $\gamma_c \in [8-14]$J.m^{-2} and $\sigma_c \in [750-1250]$MPa. Theses ranges are centered on the estimates obtained from the analysis of Fig. 17, and a ±25% is considered to assess the effect of the variation of σ_c and γ_c on the simulation results and on the comparison with experimental data. A typical output of such simulation is shown in Fig. 18. Path-following technique allows to get the solid line in Fig. 18a, corresponding to the successive equilibrium positions by which the system goes through during the cracking process, hence represent the real crack path / load-displacement curve, including the snap-back characterized by a decreasing load / decreasing displacement as crack initiates and propagates. Complete fracture corresponds to the point marked by a star and shown in Fig. 18b. Under displacement control, as in the experiments, the dotted line is obtained, with a load drop corresponding to the sudden transition between uncracked and cracked states. Key point is that, in this particular case, the elastic energy release by cracking computed with the dotted line is higher than the fracture energy that corresponds to the shaded area in Fig. 18a, thus leading to an overestimation of the fracture energy. In other word, Fig. 18a is a case where the energetic criterion is satisfied before the stress criterion, so that the failure load depends only on σ_c. Conversely, the case where the solid and dotted lines are superimposed appears when the stress criterion is satisfied but the energy criterion is yet to be fulfilled, so that failure load depends only on γ_c. For micro-beam, it has been suggested that the latter situation may be more common due to the small sizes involved [70].

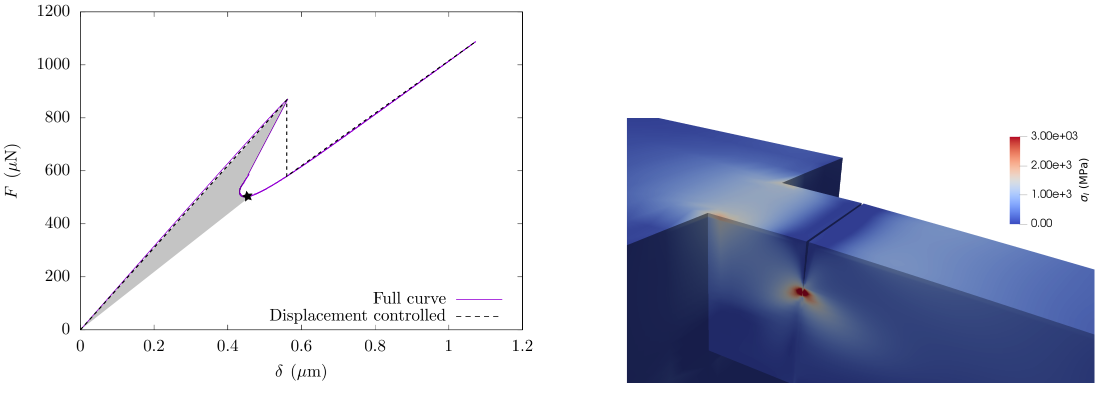

(a) (b)

Figure 18: (a) Typical load displacement curve obtained with FE simulations with CZM. Dotted line corresponds to the curve that would be obtained under displacement control. Shaded area corresponds to the fracture energy. (b) Largest principal stress field at the point marked by a star in (a).

In order to compare experimental and numerical load displacement curves unambiguously, simulations are performed only for experimental conditions fulfilling the following conditions: available crystallographic orientations (Tab. 6), clear load drop associated to cracking (Fig. 13), GBs far away enough from the fixed end ($d \gtrsim h$) with inclinations mostly perpendicular to the beam axis ($\theta \approx 0$) (Tab. 6). The two first conditions allow meaningful comparisons between numerical predictions and experimental results, while the last two ensure that cracking occurs mostly in opening mode, *i.e.*, with minimal shear, justifying to use the CZM model (Eq. 3). The simulations have thus been run for Micro-beam4-ox7470h, Micro-beam5-ox3680h, Micro-beam6-ox3680h and Micro-beam8-ox3680h for different fracture energy $\gamma_c \in [8-14]\text{J.m}^{-2}$ and strength $\sigma_c \in [750-1250]\text{MPa}$. The comparison between numerical and experimental load displacement curves are shown in Fig. 19. A fair agreement is observed for the elastic slopes and fracture loads, without any adjustable parameter. The agreement is especially good for Micro-beam6-ox3680h where the surface oxide is flat and homogeneous. Deviations from the experimental data are observed for the other cases, especially on Micro-beam4-ox7470h (Fig. 19a,b) where the oxide morphology is heterogeneous. The experimental values are in or close to the ranges predicted by numerical simulations. This is all the more remarkable given that the elastic energy release per unit cracking surface and maximal stress in the oxide obtained in Fig. 17 spans $\Delta\mathcal{E}_{el}/S_c \in [5-13]\text{J.m}^{-2}$ and $\sigma_I^{max} \in [1700-2600]\text{MPa}$, emphasizing that, as stated before, these quantities are only estimates of the fracture properties.

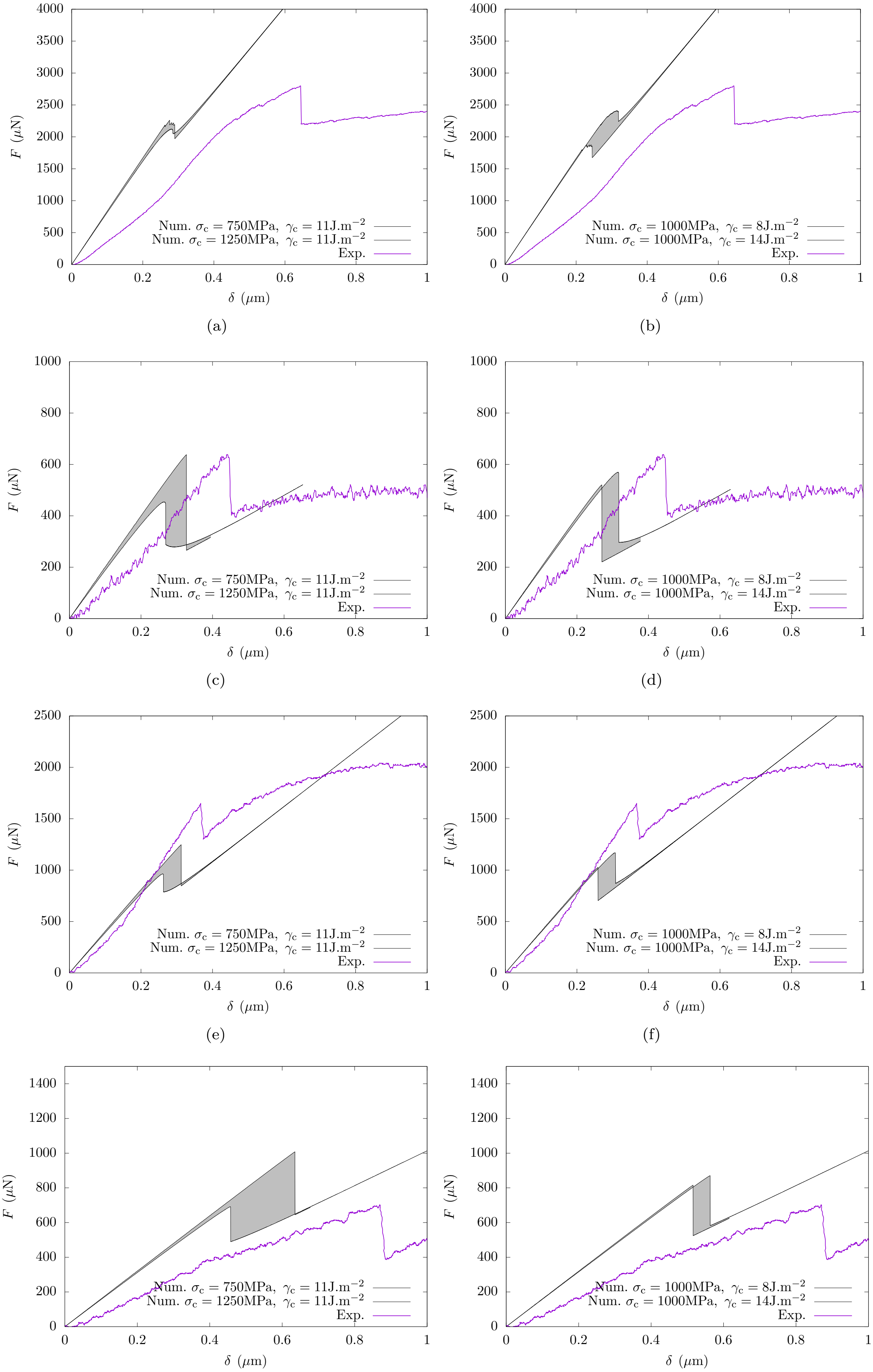

(a) (b) (c) (d) (e) (f) (g) (h)

Figure 19: Comparison of the CZM simulations curves with σ_c=[750, 1000, 1250]MPa and γ_c=[8, 11, 14]J/m^2 and experimental data (a)-(b) Micro-beam4-ox7470h (c)-(d) Micro-beam5-ox3680h (e)-(f)Micro-beam6-ox3680h (g)-(h)Micro-beam8-ox3680h

A closer look indicates that the two limiting cases described previously - γ_c-controlled *vs.* σ_c-controlled fracture - are observed. Changing σ_c does not have an effect on the numerical curves for Micro-beam4-7470h (Fig. 19a) while changing γ_c does (Fig. 19b). This γ_c-controlled fracture indicates that a higher value of fracture energy reduces the difference between experimental and numerical fracture load, for $\sigma_c = 1000\text{MPa}$. This also supports the assumption that the true fracture energy is higher than the minimal value reported in Fig. 17a. Conversely, Micro-beam8-ox3680h (Fig. 19g,h) corresponds mostly to a σ_c-controlled fracture (similar to the situation depicted in Fig. 18a) where the energy criterion is fulfilled before the stress criterion. This σ_c-controlled fracture indicates a better agreement between experimental and numerical fracture load for lower strength, for $\gamma_c = 11\text{J.m}^{-2}$. The two other cases (Micro-beam5-ox3680h (Fig. 19c,d) and Micro-beam6-ox3680h (Fig. 19e,f)) correspond to situations where both γ_c and σ_c affect fracture load. The fact that the experimental database covers both γ_c-controlled and σ_c-controlled fracture prevents the parameters of the CZM to be undetermined, which provides confidence regarding the ranges of σ_c and γ_c obtained for the fracture properties of the oxide.

In summary, the numerical simulations performed by considering a fracture energy $\gamma_c \approx 11 \pm 3\text{J.m}^{-2}$ and a strength $\sigma_c \approx 1000 \pm 250\text{MPa}$ lead to a fair agreement with experimental data regarding both fracture load and load drop, encompassing the real values for three out of four micro-beams. Interestingly, these three beams correspond to cases of metal / oxide fracture, indicating that the fracture properties obtained are better suited for that case. No attempt was made to optimize γ_c and σ_c as conflicting tendencies are observed in Fig. 19. These values are thus considered as the best estimates that can be extracted from the experimental data. In the next section, these values are first assessed with respect to their dependence to the experimental and numerical parameters, and then compared to the results available in the literature.

4. Discussion

In the following paragraphs, we discuss the values of critical strength and fracture energy that we obtained using combined experimental and numerical paths. On the experimental side, apart from the difficulties already mentioned to measure precisely the surface of the crack associated with load drops, the presence of the outer oxide layer and / or crystallites may also influence the results of the tests, as shown in [48]. On the one hand, multiple cracking (Fig. 6b) can complicate the estimation of fracture surface associated with load drop. On the other hand, numerical simulations account for the oxide layer in a simplified way - with a constant average thickness e_{ox} (Fig. 8) - affecting the comparisons between experiments and numerical predictions. Some micro-beams do have a relatively smooth and / or thin outer oxide layer, either by chance like Micro-beam6-ox3680h and Micro-beam8-ox3680h or on purpose like Micro-beam4-ox7470h (See Section 2.3). Micro-beam5-ox3680h on the other hand exhibits a more heterogeneous outer oxide layer.

Fracture has been observed to occur either inside the intergranular oxide or at the metal / oxide interface. A natural question is the physical origin of the fracture location, or put another way, why these two locations can happen. Some insights can be gained by looking at the stress profile along the beam axis (Fig. 20). Beam theory predicts a linear decrease of principal stress σ_I from the fixed end to the free end of the micro-cantilever. When accounting for the effect of the beam geometry but still using an isotropic material, the decrease of the principal stress σ_I is still linear away from the fixed end. However when the elastic mismatch between the intergranular oxide and the grains are taken into account, a more complex evolution of the principal stress σ_I is found. In particular, maxima are found at the metal / oxide interface and within the oxide. This provides a rationale for the occurrence of fracture either in the intergranular oxide or at the metal / oxide interface.

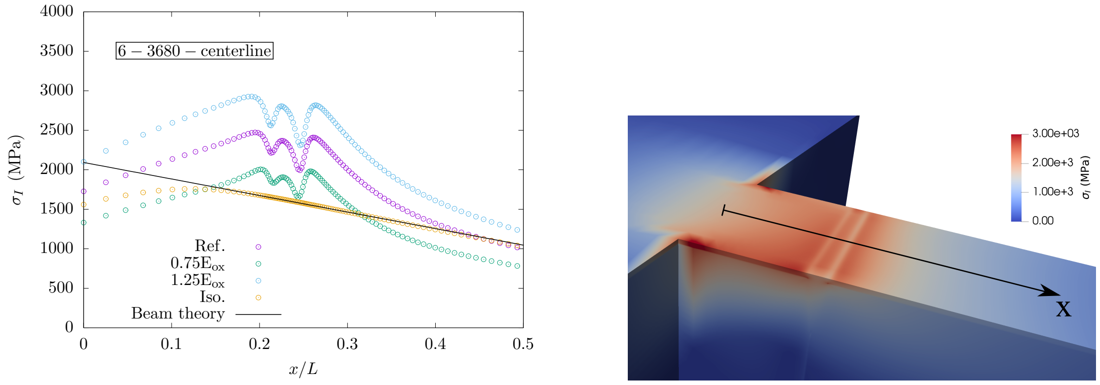

(a) (b)

Figure 20: (a) Maximal principal stress σ_I at the surface along the centerline of the beam, for Micro-beam6-3680h for various modelling strategies: FE simulations with different Young's modulus for the oxide and anisotropic elasticity for the grains, FE simulation with isotropic elasticity for the whole beam, analytical beam theory (b) Maximal principal stress field

On the numerical side, Fig. 20a also shows the effect of the oxide properties on the estimation of the maximal principal stress σ_I. In addition to the reference result using the oxide Young's modulus E_{ox} detailed in Section 2.3, two other simulations have been performed considering $0.75E_{ox}$ and $1.25E_{ox}$. A strong effect is observed on local stresses, where the higher the Young's modulus of the oxide, the higher the local stresses, due to the fact that the adjacent grains are basically imposing the deformation to the intergranular oxide. Note that, for a given applied load, changing the elastic parameters of the grains in the same way as the Young's modulus of the oxide does not change the local stresses, showing that only the elastic mismatch matters. This shows how important it is to have reliable estimates of the elastic parameters of both grains and oxide. These parameters have been obtained in this study from reliable data but in an indirect way. Performing nano-indentation could be a way to get direct estimation of the elastic parameters, even though challenging due to the shallowness of the oxide and of the anisotropy of the grains.

The fracture properties obtained in this study can be compared to the data available in the literature. As stated in the introduction, there is very few results in the literature on the fracture properties of spinel oxides on austenitic stainless steels neither from experimental studies nor numerical simulations. Moreover, no data corresponds to the exact chemical composition of the intergranular oxide of this study $(Ni_{0.7}Si_{0.5}Ca_{0.2}Zn_{0.2})(FeCr)O_4$. Comparison are made with the few available data for $NiCr_2O_4$ and $FeCr_2O_4$. For the fracture energy γ_c, values ranges from about 2J.m^{-2} to about 11J.m^{-2} from theoretical and numerical predictions [42, 43]. A value of 3.4J.m^{-2} has been reported by Dugdale et al. [47] for an oxidized GB of Inconel 600 alloy. The value obtained in this study of about 10J.m^{-2} falls within the upper range of these data. For the oxide strength σ_c, theoretical and numerical studies lead to values of a few (tens) of GPa. However, these studies consider perfect spinels, *i.e.*, without defects, hence probably not relevant for real oxides. Experimental evaluations for oxidized GBs of Inconel 600 in PWR environment lead values ranging from 575MPa [48] to 1350MPa [47]. Again the value obtained in this study of about 1000MPa falls within the range obtained in these studies. As the chemical compositions are different, this may indicate that the dependence of fracture properties of these oxides to the chemical composition is weak, but more studies are required to assess this point in more details. Additional comparisons can be made between the fracture properties γ_c and σ_c to oxide fracture stress σ_f used in numerical simulations for the fracture of PWR oxidized GB in Inconel 600. Considering an oxide of depth h_{ox} subjected to a local stress σ, fracture occurs if $\sigma \geq \sigma_c$ (stress criterion) and if the elastic energy release $(\sigma^2/E)h_{ox}^2$ is higher than fracture energy $\gamma_c h_{ox}$, hence $\sigma \gtrsim \sqrt{E\gamma_c/h_{ox}}$ (energy criterion). The fracture stress is thus $\sigma_f \approx \max\left(\sigma_c, \sqrt{E\gamma_c/h_{ox}}\right)$. A fracture stress of $\sigma_f = 900$MPa has been proposed in [39] for an oxide depth of 300nm, which leads to $\sigma_c \lesssim 900$MPa and $\gamma_c \lesssim 1$J.m^{-2}. This critical stress is consistent with previous values, but the fracture energy is smaller. Note however that simplifications have been made in [39] to estimate local stresses.

5. Conclusions and Perspectives

In this study, the fracture properties of a $FeCr_{12}Ni_{26}Si_3$ austenitic stainless steel grain boundaries oxidized in PWR environment have been assessed through bending tests on micro-cantilever beams at room temperature. The main results are as follows:

- The $FeCr_{12}Ni_{26}Si_3$ alloy selected to emulate the chemical composition of 304 / 316 stainless steels grain boundaries after irradiation has been confirmed to be susceptible to IGSCC in PWR environment with a SSRT test. This susceptibility is supposed to be related to the low Cr / high Si content according to data available in the literature.

- Oxidation experiments in PWR environment up to 7470h lead to a micron-scale duplex oxide layer with intergranular oxide penetration up to 1.3μm deep. The chemical composition measured by TEM-EDS analysis are $(Ni_{0.9}, Fe_{1.6})Fe_2O_4$ for the outer layer and $(Ni_{0.7}Si_{0.5}Ca_{0.2}Zn_{0.2})(FeCr)O_4$ for the inner layer and intergranular oxide.

- 16 bending tests on micro-cantilever beams containing a single oxidized grain boundary have been carried out in-situ SEM at room temperature. 12 tests have led to fracture either at the metal / oxide interface (7/12) or inside the intergranular oxide (5/12). Analytical and numerical evaluations of elastic energy release per unit cracking area - an estimate of fracture energy - and maximal stress in the intergranular oxide - an estimate of oxide strength - lead to $[2-16]$J.m^{-2} and $[800-2600]$MPa, respectively.

- Finite Element simulations with CZM elements have been performed for selected experimental conditions. A good agreement is obtained for fracture loads and load drops considering a fracture energy $\gamma_c = 11 \pm 3$J.m^{-2} and a strength $\sigma_c = 1000 \pm 250$MPa. These values appear more suited for fracture occurring at the metal / oxide interface.

- The fracture properties obtained are in qualitative agreement with experimental data obtained on Inconel 600 that forms similar oxides in PWR environment.

Two main perspectives can be identified to extend this work in order to support the use of these fracture properties in the modelling of IGSCC / IASCC of austenitic stainless steels. First, as stated in Section 4, performing and interpreting these micro-cantilever bending tests remain a challenge due to both experimental and numerical difficulties. More experiments are thus needed, with a special care taken to perform tests easier to analyze - for example by removing the outer oxide layer, selecting GB perpendicular to the top surface - and to assess properly all properties needed to perform the simulations such as the elastic parameters of oxides and grains. Alternative modeling of fracture [71] could also be considered, in which crack path is the result of the simulations and not set a priori as with the CZM model. The second perspective would be to assess the effect of temperature on fracture properties as IASCC of austenitic stainless steels of PWR internal structures appears at a temperature of about 300°C.

Acknowledgements

The authors thank Florian Le Bourdais for the RUS measurements, Matthias Rousseau for the SSRT test and oxydation experiments. Cecile Marcelot from CEMES (CNRS) and the staff LECI (CEA) are also greatly acknowledged.

Appendix A

Tab. 6 summarizes the geometrical parameters defined in Fig. 8 for the micro-beams where fracture occurred.

	$\boldsymbol{d_1}$ (μm)	$\boldsymbol{d_2}$ (μm)	$\boldsymbol{\theta}$	$\boldsymbol{w_{ox}}$ (μm)	$\boldsymbol{e_{ox}}$ (μm)	$\boldsymbol{X_1}$	$\boldsymbol{Y_1}$	$\boldsymbol{X_2}$	$\boldsymbol{Y_2}$
Micro-beam1-ox3680h	1.8	1.6	-20	0.2	0.2	-	-	-	-
Micro-beam2-ox3680h	4.0	3.7	40	0.6	0.2	-	-	-	-
Micro-beam3-ox3680h	4.3	4.7	15	0.2	0.1	-	-	-	-
Micro-beam4-ox3680h	3.0	2.2	33	0.5	0.3	-	-	-	-
Micro-beam5-ox3680h	1.4	1.7	10	0.2	0.1	$[7\,9\,\bar{5}]$	$[\bar{1}\,\bar{5}\,\overline{11}]$	$[\bar{5}\,\bar{6}\,7]$	$[\bar{9}\,\bar{4}\,\overline{10}]$
Micro-beam6-ox3680h	2.7	2.6	0	0.4	0.1	$[\bar{3}\,0\,2]$	$[\bar{5}\,\bar{6}\,\bar{7}]$	$[2\,5\,\bar{2}]$	$[\bar{9}\,\bar{1}\,\overline{12}]$
Micro-beam7-ox3680h	2,8	2.7	55	0.4	0.1	$[\overline{10}\,\bar{9}\,6]$	$[4\,1\,9]$	$[\bar{3}\,\overline{11}\,2]$	$[\bar{2}\,0\,\bar{3}]$
Micro-beam8-ox3680h	1.3	1.9	32	0.9	0.3	$[3\,11\,\overline{10}]$	$[\bar{2}\,\bar{3}\,\bar{4}]$	$[\overline{12}\,\bar{3}\,7]$	$[\bar{6}\,\bar{2}\,\overline{11}]$
Micro-beam4-ox7470h	1.0	0.7	16	0.5	0.3	$[\bar{1}\,\overline{11}\,7]$	$[\bar{5}\,\bar{6}\,\overline{10}]$	$[\overline{11}\,2\,3]$	$[\bar{3}\,\bar{1}\,\overline{12}]$
Micro-beam5-ox7470h	0.8	3.5	-47	1.4	0.2	$[\bar{4}\,\bar{7}\,7]$	$[9\,6\,11]$	$[9\,\bar{6}\,\bar{4}]$	$[2\,1\,3]$
Micro-beam6-ox7470h	2.4	3.7	-25	0.2	0.1	$[\bar{6}\,\overline{12}\,11]$	$[9\,6\,11]$	$[4\,7\,\bar{4}]$	$[2\,5\,11]$
Micro-beam8-ox7470h	2.5	2.0	-45	0.8	0.1	$[\bar{2}\,5\,1]$	$[\bar{6}\,\bar{1}\,\bar{8}]$	$[\bar{1}\,12\,\bar{1}]$	$[\bar{8}\,\bar{1}\,\overline{10}]$

Table 6: Geometrical parameters defining the position of the grain boundary (d_1, d_2 and θ), the width w_{ox} of the intergranular oxide and average thickness of the surface oxide layer e_{ox}. X_i and Y_i corresponds to the axis defined in Fig. 8 written in the crystal frame.

References

[1] TD Burleigh. The postulated mechanisms for stress corrosion cracking of aluminum alloys: A review of the literature 1980-1989. *Corrosion*, 47(2):89–98, 1991.

[2] MA Arafin and JA Szpunar. A new understanding of intergranular stress corrosion cracking resistance of pipeline steel through grain boundary character and crystallographic texture studies. *Corrosion Science*, 51(1):119–128, 2009.

[3] R.W. Staehle. Quantitative micro-nano (QMN-2) approach to predicting SCC of Fe-Cr-Ni alloys—initiation of SCC. In *Proceedings of Workshop Held at Sun Valley Resort*, 2011.

[4] A. King, G. Johnson, D. Engelberg, W. Ludwig, and J. Marrow. Observations of intergranular stress corrosion cracking in a grain-mapped polycrystal. *Science*, 321:382–385, 2008.

[5] IAEA. Stress corrosion cracking in light water reactors: Good practices and lessons learned. NP-T-3.13, IAEA Nuclear Energy Series, 2011.

[6] F. Cattant. *Materials Ageing in Light-Water Reactors*. Springer, 2022.

[7] R.B. Rebak. Stress corrosion cracking (SCC) of nickel-based alloys. pages 273–306. Elsevier, 2011.

[8] Steve Fyfitch. Corrosion and Stress Corrosion Cracking of Ni-Base Alloys. In Rudy J.M. Konings and Roger E. Stoller, editors, *Comprehensive Nuclear Materials (Second Edition)*, pages 96–117. Elsevier, Oxford, second edition edition, 2020.

[9] V. Kain. Stress corrosion cracking (SCC) in stainless steels. In *Stress corrosion cracking*, pages 199–244. Elsevier, 2011.

[10] U. Ehrnsten. Corrosion and Stress Corrosion Cracking of Austenitic Stainless Steels. In Rudy J.M. Konings and Roger E. Stoller, editors, *Comprehensive Nuclear Materials (Second Edition)*, pages 118–128. Elsevier, Oxford, second edition edition, 2020.

[11] F. Cattant. Stress corrosion cracking of cold worked stainless steels. In *Materials Ageing in Light-Water Reactors*, pages 739–835. Springer, 2022.

[12] F. Cattant. Stress corrosion cracking of stainless steel in polluted environment or in occluded conditions. In *Materials Ageing in Light-Water Reactors*, pages 881–1106. Springer, 2022.

[13] ASN. `https://www.french-nuclear-safety.fr/asn-informs/news-releases/stress-corrosion-phenomenon-asn-asks-edf-for-more-`

[14] NRC. `https://www.nrc.gov/reactors/operating/ops-experience/baffle-former-bolts.html`.

[15] O. K. Chopra and A. S. Rao. A review of irradiation effects on LWR core internal materials - IASCC susceptibility and crack growth rates of austenitic stainless steels. *Journal of Nuclear Materials*, 409(3):235 – 256, 2011.

[16] F. Cattant. Stainless steels IASCC. In *Materials Ageing in Light-Water Reactors*, pages 839–880. Springer, 2022.

[17] S. M. Bruemmer, E. P. Simonen, P. M. Scott, P. L. Andresen, G. S. Was, and J. L. Nelson. Radiation-induced material changes and susceptibility to intergranular failure of light-water-reactor core internals. *Journal of Nuclear Materials*, 274(3):299–314, 1999.

[18] D. Edwards, E. P. Simonen, and S. M. Bruemmer. Evolution of fine-scale defects in stainless steels neutron-irradiated at 275°C. *Journal of Nuclear Materials*, 317:13–31, 2003.

[19] O.K. Chopra and A.S. Rao. A review of irradiation effects on LWR core internal materials - neutron embrittlement. *Journal of Nuclear Materials*, 412(1):195–208, 2011.

[20] G. S. Was. Localized deformation as a primary cause of irradiation assisted stress corrosion cracking. Technical report, University of Michigan, 2009.

[21] P. Deng, Q. Peng, E.-H. Han, W. Ke, C. Sun, and Z. Jiao. Effect of irradiation on corrosion of 304 nuclear grade stainless steel in simulated PWR primary water. *Corrosion Science*, 127:91–100, 2017.

[22] M. Boisson, L. Legras, E. Andrieu, and L. Laffont. Role of irradiation and irradiation defects on the oxidation first stages of a 316L austenitic stainless steel. *Corrosion Science*, 161:108194, 2019.

[23] C. Pokor, G. Courtemanche, J.L. Flejou, M. Tommy-Martin, I. Rupp, B. Tanguy, J.P. Massoud, and N. Monteil. IASCC of Core Internals of PWRs: EDF R&D and Engineering program to assess internals lifetime management. volume Proceedings of the International Symposium Fontevraud VII, September 2010.

[24] S. Fyfitch, S. Davidsaver, and K. Amberge. Irradiation-assisted stress corrosion cracking initiation screening criteria for stainless steels in PWR systems. In *Proceedings of the 18th International Conference on Environmental Degradation of Materials in Nuclear Power Systems – Water Reactors*, 2017.

[25] M. J. Konstantinović. Probabilistic fracture mechanics of irradiation assisted stress corrosion cracking in stainless steels. *Procedia Structural Integrity*, 2:3792 – 3798, 2016. 21st European Conference on Fracture, ECF21, 20-24 June 2016, Catania, Italy.

[26] A.G. Penders, M.J. Konstantinovic, W. Van Renterghem, R-W. Bosch, D. Schryvers, and F. Somville. Characterization of IASCC crack tips extracted from neutron-irradiated flux thimble tube specimens in view of a probabilistic fracture model. *Journal of Nuclear Materials*, 571:154015, 2022.

[27] L. Cizelj and H. Riesch-Oppermann. Towards growth model for short intergranular cracks in elastoplastic polycrystalline aggregate. volume Proceedings of the International Symposium Fontevraud V, pages 196–203, September 2002.

[28] F. Barbe, S. Forest, and G. Cailletaud. Intergranular and intragranular behavior of polycrystalline aggregates. Part 1: F.E. model. *Int. J. Plasticity*, 17:513–536, 2001.

[29] F. Roters, P. Eisenlohr, L. Hantcherli, D. D. Tjahjanto, T. R. Bieler, and D. Raabe. Overview of constitutive laws, kinematics, homogenization and multiscale methods in crystal plasticity finite-element modeling: Theory, experiments, applications. *Acta Materialia*, 58(4):1152–1211, 2010.

[30] Alisa Stratulat, Jonathan A. Duff, and T. James Marrow. Grain boundary structure and intergranular stress corrosion crack initiation in high temperature water of a thermally sensitised austenitic stainless steel, observed in situ. *Corrosion Science*, 85:428–435, 2014.

[31] E.A. West and G.S. Was. A model for the normal stress dependence of intergranular cracking of irradiated 316L stainless steel in supercritical water. *Journal of Nuclear Materials*, 408(2):142–152, 2011.

[32] Igor Simonovski and Leon Cizelj. Cohesive zone modeling of intergranular cracking in polycrystalline aggregates. *Nuclear Engineering and Design*, 283:139 – 147, 2015.

[33] Qi Huang, Y. Charles, Cecilie Duhamel, Monique Gaspérini, and Jérôme Crépin. Influence of the Combination of Microstructure and Mechanical Fields on Stress Corrosion Cracking Initiation of Cold-Worked Austenitic Stainless Steels. In *19th International Conference on Environmental Degradation of Materials in Nuclear Power Systems-Water Reactor*, pages 967–978, 2019.

[34] Qi Huang, Yann Charles, Marc Maisonneuve, Cécilie Duhamel, Catherine Guerre, Monique Gaspérini, and Jérôme Crepin. Experimental and numerical analysis of mechanical fields on cross-shaped specimens for stress corrosion cracking of cold-worked austenitic stainless steels exposed to primary environment. *Journal of Nuclear Materials*, 582:154478, 2023.

[35] D. Liang, J. Hure, A. Courcelle, S. El Shawish, and B. Tanguy. A micromechanical analysis of intergranular stress corrosion cracking of an irradiated austenitic stainless steel. *Acta Materialia*, 204:116482, 2021.

[36] Pierre Evrard and Maxime Sauzay. Modelling of the effect of dislocation channel on intergranular microcrack nucleation in pre-irradiated austenitic stainless steels during low strain rate tensile loading. *Journal of Nuclear Materials*, 405(2):83–94, 2010.

[37] M. Sauzay and M. O. Moussa. Prediction of grain boundary stress fields and microcrack initiation induced by slip band impingement. *International Journal of Fracture*, 184(1-2):215–240, 2013.

[38] T. Couvant, D. Haboussa, S. Meunier, G. Nicolas, E. Julan, K. Sato, and F. Delabrouille. A simulation of IGSCC of austenitic stainless steels exposed to primary water, in. In *17th International Conference on Environmental Degradation of Materials in Nuclear Power Systems-Water Reactors, Ottawa, CA, August 9–13*, pages 1987–2008, 2015.

[39] T. Couvant, J. Caballero, C. Duhamel, J. Crépin, and T. Maeguchi. Calibration of the local IGSCC engineering model for alloy 600. In *Proceedings of the 18th International Conference on Environmental Degradation of Materials in Nuclear Power Systems–Water Reactors*, pages 1511–1533. Springer, 2019.

[40] R.P. Matthews, R.D. Knusten, J.E. Westraadt, and T. Couvant. Intergranular oxidation of 316L stainless steel in the PWR primary water environment. *Corrosion Science*, 125:175–183, 2017.

[41] Shengkai Wang, Shihao Zhang, Jiayu Xie, Miao Song, and Wenjun Kuang. The time dependence of proton irradiation effect on the intergranular oxidation of 316L stainless steel in high-temperature hydrogenated water. *Acta Materialia*, 260:119340, 2023.

[42] D Tromans and J.A Meech. Fracture toughness and surface energies of minerals: theoretical estimates for oxides, sulphides, silicates and halides. *Minerals Engineering*, 15(12):1027–1041, 2002.

[43] L. Van Brutzel. Calcul des propriétés mécaniques des spinelles de corrosion. *Private communication*, 2021.

[44] S. Brinckmann, K. Matoy, C. Kirchlechner, and G. Dehm. On the influence of micro-cantilever pre-crack geometries on the apparent fracture toughness of brittle materials. *Acta Materialia*, 136:281–287, 2017.

[45] D. E. J. Armstrong, M. E. Rogers, and S. G. Roberts. Micromechanical testing of stress corrosion cracking of individual grain boundaries. *Scripta Materialia*, 61(7):741–743, 2009.

[46] Y. Takahashi, H. Kondo, R. Asano, S. Arai, K. Higuchi, Y. Yamamoto, S. Muto, and N. Tanaka. Direct evaluation of grain boundary hydrogen embrittlement: A micro-mechanical approach. *Materials Science and Engineering: A*, 661:211–216, 2016.

[47] H. Dugdale, D. E. J. Armstrong, E. Tarleton, S. G. Roberts, and S. Lozano-Perez. How oxidized grain boundaries fail. *Acta Materialia*, 61(13):4707–4713, 2013.

[48] J. Dohr, D. E. J. Armstrong, E. Tarleton, T. Couvant, and S. Lozano-Perez. The influence of surface oxides on the mechanical response of oxidized grain boundaries. *Thin Solid Films*, 632:17–22, 2017.

[49] A. Stratulat, D. E. J. Armstrong, and S. G. Roberts. Micro-mechanical measurement of fracture behaviour of individual grain boundaries in Ni alloy 600 exposed to a pressurized water reactor environment. *Corrosion Science*, 104:9–16, 2016.

[50] K. Fukuya. Current understanding of radiation-induced degradation in light water reactor structural materials. *Journal of Nuclear Science and Technology*, 50:213–254, 2013.

[51] M Nastar and F Soisson. Radiation-Induced Segregation. In Rudy J.M. Konings and Roger E. Stoller, editors, *Comprehensive Nuclear Materials (Second Edition)*, pages 235–264. Elsevier, Oxford, second edition edition, 2020.

[52] R.E. Schramm and R.P. Reed. Stacking fault energies of seven commercial austenitic stainless steels. *Metallurgical Transactions A*, 6(7):1345–1351, 1975.

[53] F. Bachmann, R. Hielscher, and H. Schaeben. Texture analysis with MTEX–free and open source software toolbox. In *Solid state phenomena*, volume 160, pages 63–68. Trans Tech Publ, 2010.

[54] Rachma Azihari, Jeremy Hure, Marc Legros, and Benoit Tanguy. Micro-mechanical approach of the intergranular stress corrosion cracking of austenitic stainless steels in pwr environment. 2022.

[55] N. Sakaguchi, M. Endo, S. Watanabe, H. Kinoshita, S. Yamashita, and H. Kokawa. Radiation-induced segregation and corrosion behavior on Σ3 coincidence site lattice and random grain boundaries in proton-irradiated type-316L austenitic stainless steel. *Journal of Nuclear Materials*, 434(1-3):65–71, 2013.

[56] J.M. Scherer, J. Hure, R. Madec, F. Le Bourdais, L. van Brutzel, S. Sao-Joao, G. Kermouche, J. Besson, and B. Tanguy. Tensile and micro-compression behaviour of AISI 316L austenitic stainless steel single crystals at 20°C and 300°C: experiments, modeling and simulations. *submitted*, -:–, 2023.

[57] J. M. Bussey, M. H. Weber, N. J. Smith-Gray, J. J. Sly, and J. S. McCloy. Examining phase separation and crystallization in glasses with X-ray nano-computed tomography. *Journal of Non-Crystalline Solids*, 600:121987, 2023.

[58] A.A. Griffith. The phenomena of rupture and flow in solids. *Philosophical Transactions of the Royal Society of London A*, 221:163–198, 1921.

[59] D. Leguillon. Strength or toughness? a criterion for crack onset at a notch. *European Journal of Mechanics-A/Solids*, 21(1):61–72, 2002.

[60] R. F. S. Hearmon. The elastic constants of anisotropic materials. *Rev. Mod. Phys.*, 18:409–440, Jul 1946.

[61] H. M. Ledbetter. Monocrystal-polycrystal elastic constants of a stainless steel. *physica status solidi (a)*, 85(1):89–96, 1984.

[62] L. Van Brutzel. Private communication, 2023.

[63] CEA. Cast3M. *www-cast3M.cea.fr*, 2022.

[64] V. Tvergaard. Effect of fibre debonding in a whisker-reinforced metal. *Materials science and engineering: A*, 125(2):203–213, 1990.

[65] K. Park and G.H. Paulino. Cohesive zone models: A critical review of traction-separation relationships across fracture surfaces. *Journal of Applied Mechanics*, 64:060802, 2013.

[66] J. Gupta, J. Hure, B. Tanguy, L. Laffont, M.-C. Lafont, and E. Andrieu. Characterization of ion irradiation effects on the microstructure, hardness, deformation and crack initiation behavior of austenitic stainless steel:heavy ions vs protons. *Journal of Nuclear Materials*, 501:45–58, 2018.

[67] M. Le Millier, O. Calonne, J. Crépin, C. Duhamel, L. Fournier, F. Gaslain, E. Héripré, O. Toader, Y. Vidalenc, and G. Was. Influence of strain localization on IASCC of proton irradiated 304L stainless steel in simulated PWR primary water. In *16th International Conference on Environmental Degragation of Materials in Nuclear Power Systems - Water Reactors*, 2013.

[68] S. E. Ziemniak, M. Hanson, and P. C. Sander. Electropolishing effects on corrosion behavior of 304 stainless steel in high temperature, hydrogenated water. *Corrosion Science*, 50(9):2465–2477, 2008.

[69] G. Han, Z. Lu, X. Ru, J. Chen, J. Zhang, and T. Shoji. Properties of oxide films formed on 316l ss and model alloys with modified ni, cr and si contents in high temperature water. *Corrosion Science*, 106:157–171, 2016.

[70] Sara Jimenez-Alfaro and Dominique Leguillon. Finite fracture mechanics at the micro-scale. application to bending tests of micro cantilever beams. *Engineering Fracture Mechanics*, 258:108012, 2021.

[71] S. Jimenez-Alfaro, J. Reinoso, D. Leguillon, and C. Maurini. Finite fracture mechanics from the macro- to the micro-scale. comparison with the phase field model. *Procedia Structural Integrity*, 42:553–560, 2022. 23 European Conference on Fracture.